Developmental variability in cotton fiber cell wall properties linked to important agronomic traits

Michael C. Wilson[1], Alexander H. Howell[2,3], Anika Sood[4], Youngwoo Lee[2,3], Pengcheng Yang[5], Elena Yu[3], Heena Rani[2,3,†], Eileen L. Mallery[2,3], Sivakumar Swaminathan[6], Corrinne E. Grover[7], Jonathan F. Wendell[7], Olga A. Zabotina[6], Jun Xie[5], Chelsea S. Davis[1,8,9], Daniel B. Szymanski[2,3*]

[1]School of Materials Engineering, Purdue University, West Lafayette, IN 47907, USA
[2]Center for Plant Biology, Purdue University, West Lafayette, IN 47907, USA
[3]Department of Botany and Plant Pathology, Purdue University, West Lafayette, IN 47907, USA
[4]Department of Biological Sciences, Purdue University, West Lafayette, IN 47907, USA
[5]Department of Statistics, Purdue University, West Lafayette, IN 47907, USA
[6]Roy J. Carver Department of Biochemistry, Biophysics, and Molecular Biology, Iowa State University, Ames, IA 50011, USA
[7]Department of Ecology, Evolution, and Organismal Biology, Iowa State University, Ames, IA 50011, USA
[8]Department of Mechanical Engineering, University of Delaware, Newark, DE 19716, USA.
[9]Department of Materials Science and Engineering, University of Delaware, Newark, DE 19716, USA.

[†]Present address: USDA-ARS, Cereal Crops Research Unit, Madison, WI 53726, USA

[*]Corresponding Author: szymandb@purdue.edu

Short Title: Analyses of Cotton Fiber Morphogenesis

Keywords: cotton, multiscale phenotyping, CESA, cellulose, morphogenesis, finite element modeling

ABSTRACT

The economic value of cotton is based on long, thin, strong, and twisted trichoblast cells that emerge from the ovule epidermis. The mature dried cell reflects the final outcome of a complicated morphogenesis process that includes rapid tapering of the nascent trichoblast, weeks of polarized diffuse growth, followed by a transition to persistent secondary cell wall synthesis. Cellulose microfibril-based anistropic growth control is central to this process. It is widely assumed that the transition to secondary wall synthesis causes a reduced growth rate. However, the biomechanical details that directly link cell wall properties, with fiber morphogenesis is very poorly understood. In this paper, we developed novel imaging quantitative phenotyping, and computational modeling pipelines to analyze fiber growth at a daily resolution. We uncovered unexpected variability in growth rate, cell wall properties, and cell geometry across a broad developmental window. Finite element computational modeling of fiber growth was used to predict how spatial gradients of fiber and matrix material properties can interact to dictate the patterns of shape change. Cellulose patterning is central to the

developmental process, and as an initial step toward gaining insight into the molecular control the expression profiles of a broad set of genes known to orchestrate cellulose biosynthesis were quantified across the same developmental timeline and correlated with fiber phenotypes. This analysis identified specific *Gossypium hirsutum* targets for fiber quality improvement.

INTRODUCTION

The widely grown cottons *G.hirsutum* (*G.h.*) and *G.barbadense* (*G.b.*) rank among the world's most economically important crop species and provide the largest source of renewable textiles ($6.3 billion in raw product, FAOSTAT, http://www.fao.org). This global economy is based solely on the growth and morphogenesis of individual fiber cells that emerge from the developing seed coat and generate a spinnable fiber cell dominated by the properties of crystalline cellulose in the cell wall (Martinez-Sanz, et al., 2017). Given recent advances in knowledge and technologies to analyze cell shape control (Bidhendi and Geitmann, 2018; Gu and Rasmussen, 2022; Yanagisawa, et al., 2022), there are numerous opportunities to use systems level data and computational modeling of cell shape to guide the engineering of cotton with improved agronomic value. In this paper, the spatio-temporal control of growth and cellulose patterning was quantitatively analyzed at unprecedented resolutions and provides new insights into the complex growth behaviors, cell wall properties, and gene expression transitions that underlie important fiber traits.

Developing cotton fibers employ evolutionarily conserved biomechanical control mechanisms to dictate the rates and spatial patterns of growth. Cotton fibers expand through diffuse growth (Ryser, 1977; Seagull, 1986; Seagull, 1990; Tiwari and Wilkins, 1995; Yanagisawa, et al., 2022), and the growing cell continually synthesizes and modulates the material properties of a tough outer cell wall that deforms in response to turgor-driven axial and circumferential forces (Lockhart, 1965; Proseus, et al., 2000; Szymanski and Cosgrove, 2009). Polarized growth occurs because a highly organized array of cortical microtubules patterns the motility of cellulose synthase complexes in the plasma membrane (CESA). These CESA complexes synthesize aligned extracellular microfibrils comprised of bundles of 18 individual cellulose chains (Nixon, et al., 2016l; Purushotham, et al., 2020). Strong lateral associations among the aligned microfibrils generate a highly anisotropic cell wall that resists deformation parallel to the fibers and are permissive for cell expansion in an orthogonal direction (Baskin, 2005; Paredez, et al., 2006; Zhang, et al., 2021). Consequently, microfibril ordering at cellular scales drives morphogenesis patterns in cotton (Seagull, 1990; Seagull, 1992; Yanagisawa, et al., 2022).

Fiber diameter, an important agronomic trait, is first established during the distinct morphogenetic phase of cell tapering (Applequist, et al., 2001; Stiff and Haigler, 2016). The mechanism appears to be conserved, as aerial trichoblasts in many species maintain transverse microtubules along the cell flank and a microtubule-depleted zone at the cell apex that can drive tapering (Graham and Haigler, 2021; Yanagisawa, et al., 2015; Yanagisawa, et al., 2022). These microtubules pattern transverse cellulose fibers in the cells flanks and random fiber arrangements in the apex. This spatial arrangement of differing wall properties leads to a progressive reduction in cell diameter at the tip as the trichoblast elongates (Yanagisawa, et al., 2015; Yanagisawa, et al., 2022). The actin cytoskeleton is also critical for fiber development. Actin bundles have a net longitudinal arrangement developing fiber cells and is a critical roadway for long distance

intracellular transport (Yanagisawa, et al., 2022; Yu, et al., 2019). This arrangement is required for the overall organization of the cytoplasm to enable distributed secretion on the cell surface so that cell wall thickness is properly integrated with cell volume changes during growth. Genetic experiments in cotton have identified an large number of cytoskeletal proteins that are required for normal fiber growth and reinforce the overall importance of the cytoskeleton (Gilbert, et al., 2014; Li, et al., 2005; Qu, et al., 2012; Thyssen, et al., 2017; Zang, et al., 2021).

The rate and duration of cell elongation determines fiber length and partially explains the increased length of *G.b.* fibers compared to *G.h.* fibers (Avci, et al., 2013; Beasley and Ting, 1974; Schubert, et al., 1976). However, it is challenging to determine which cell properties control the rate of cell expansion. Parameters like wall thickness, turgor pressure, and matrix modulus affect growth rate, as identified in computational mechanical models of growing trichoblasts (Yanagisawa, et al., 2015; Yanagisawa, et al., 2022). Cotton fibers appear to modulate turgor during the elongation phase by switching on and off their symplastic connectivity to adjacent epidermal cells to generate a defined interval of elevated turgor (Ruan, et al., 2001). Alterations in cell wall matrix components such as pectin and hemicelluloses may also influence cell wall stiffness (Avci, et al., 2013; Meinert and Delmer, 1977; Pettolino, et al., 2022); however, the specific polysaccharides that modulate growth rate are not known. At an even more basic level, there are disagreements in the literature regarding the potential role of tip growth in fiber cells (Qin and Zhu, 2011; Yu, et al., 2019), and there is a lack of clarity about the relationship between growth rate and secondary cell wall (SCW) synthesis. It is widely assumed that growth rates slow as the cell transitions to secondary cell wall synthesis; however, direct comparisons of growth rate and the timing of secondary cell wall synthesis have not been made. The induction of SCW cellulose synthase subunit genes occurs at ~16 DPA (Betancur, et al., 2010; Pear, et al., 1996). An early study that analyzed fiber elongation rates points to a decreasing growth rate at ~11 DPA (Schubert, et al., 1973).

Regardless of whether or not SCW synthesis exerts a primary effect on growth rate, the cell undergoes massive compositional and structural rearrangements following the transition to SCW synthesis (Kumar, et al., 2016; Lyczakowski, et al., 2019; Zhong, et al., 2019). SCW CESA gene expression is activated (Betancur, et al., 2010; Haigler, et al., 2009; Pear, et al., 1996), as part of a broader transcriptional rewiring of gene expression in which 40% of expressed genes have an altered expression level as the cell transitions to SCW synthesis(Grover, et al., 2024). The orientations of both microtubules and microfibrils switch from net transverse to a longitudinally-biased spiraled configuration (Seagull, 1986; Seagull, 1992). In general, the means by which the cortical microtubule array obtains a cellular-scale order that reflects the geometry of the cell is not known, and may include several mechanisms (Oda, 2015; Williamson, 1990; Yanagisawa, et al., 2015).

Cortical microtubules are tightly associated with the plasma membrane and can align parallel to the magnitudes and directions of in-plane stress (Belteton, et al., 2021; Hamant, et al., 2008; Hejnowicz, et al., 2000; Uyttewaal, et al., 2012). Mechanical simulations that use realistic values of wall stress based on trichoblast geometries suggest that stress-sensing can organize a transverse array and an apical microtubule depletion zone (Yanagisawa, et al., 2022). In growing *Arabidopsis* trichomes, there is a bias toward left-handed helices after the geometry of the cell is specified (Keynia, et al., 2022; Sambade, et al., 2014); however, the means by which a spiraled microtubule array forms remains mysterious. Combinations of stress sensing, cell geometry, and the self-assembling of the cellulose microfibril array may be involved (Chan and Coen, 2020; Himmelspach, et al., 2003; Paredez, et al., 2006; Zang, et al., 2021). In trichoblasts, a spiraled

microtubule and microfibril system is sufficient to pattern a cell wall that twists with the same handedness when the stored energy of the turgor-loaded wall is released (Hsieh, 2007).

This paper is part of a suite of analyses that were conducted at daily time intervals—RNAseq (Grover, et al., 2024), proteomic (Lee, unpublished), and glycomic (Swaminathan, et al., 2024)—in order to obtain a high-resolution portrait of the molecular profiles that span the elongation to SCW phases of fiber development. The multiscale phenotyping reported in this paper revealed numerous examples of temporal variability in cell wall thickness, growth rate, and microfibril organization. By associating microfibril behaviors with cell shape changes during growth, the biomechanical challenges of defining a small cell diameter during a protracted developmental program were revealed. In effect, mechanical modeling highlighted the relationships between cell wall mechanical anisotropy and tip geometry. Lastly, the cellulose synthesis gene expression network was analyzed as a test case to determine how cotton deploys specific subsets of homologous genes to execute a morphogenetic program that fuels the cotton industry.

RESULTS

Growth rate and cell wall thickness analysis

To better understand the cellular control of fiber development, data were aggregated to analyze fiber morphology and cell wall traits from the nanoscale of wall thickness to the micrometer scale of microfibril bundling to the millimeter scale of fiber length. Sampling was designed to test for phenotypic variability at daily intervals across the elongation, transition and SCW regimes of fiber development (Figure 1A). Boll and fiber measurements taken from triplicate samples of dissected bolls followed a similar pattern of progressively increasing dimension with an obvious plateau at ~15 DPA (Fig. 1B and 1C, Supplemental Table 1A,B). The mean maximum fiber length underwent a nearly five-fold change from 5-25 DPA as they elongated to ~40 mm. The fiber length data fit well to a logistic growth model (Figure 1C). To estimate the fiber growth rate, the derivative of this fitted logistic growth was calculated at points across the 5-25 DPA interval. The peak at ~11 DPA has been observed with field grown *G.h.* fibers (Schubert, et al., 1973). Because the entire cell would elongate in a diffuse growth mechanism, relative growth was divided by the mean fiber length at each sampling point. The estimated relative fiber cell expands at ~30%/day until 8 DPA, after which the relative growth rates decreased steadily to nearly zero by 20 DPA (Figure 1D, Supplemental Table 1C). The decreases in growth rate (Figure 1C and 1D) precede the expected transition to secondary cell wall synthesis at ~15 or 16 DPA. Under our growth chamber conditions, upregulation of several SCW CESA genes (Grover, et al., 2024) and an associated increases in cellulose content (Swaminathan, et al., 2024) are detected at ~14 and 16 DPA, respectively (Supplemental Figure 1).

Cell wall thickness variability can contribute to cell expansion rates (Yanagisawa, et al., 2015). To determine cell wall thickness variability, published transmission electron microscopy data were mined (Supplementary Table 2) and reliable values were aggregated across developmental time (Figure 1E and 1F). After the tapering phase is completed at ~2 DPA, wall thickness is maintained at 100-200 nm until 6 DPA, after which the wall thickness appears to abruptly double and was maintained at ~400 nm until 16 DPA (Figure 1E). Increased thickness due to SCW synthesis is apparent after 20 DPA and the rate of thickness increase appears to be

constant until maturity (Figure 1F). The daily changes in cellulose, pectin, and hemicellulose were quantified and statistically analyzed by ANOVA (Supplemental Figure 1).

Microfibril bundling and orientation quantification

The alignment of cellulose microfibrils is a key determinant of fiber shape change and twist (Keynia, et al., 2022; Seagull, 1990; Yanagisawa, et al., 2022). The microfibril orientation in *G.h.* fiber cells has been previously reported to decrease at ~11DPA (Jiang, et al., 2022), but it is not clear whether there are local variations. Here, we sought to develop a robust and quantitative confocal imaging pipeline to analyze microfibril organization and cell shape at subcellular and cellular scales. Calcofluor-stained fibers were imaged at several overlapping domains with a confocal microscope to generate a montaged image of an extended domain of individual fibers (Figure 2A). The fibers contained an obviously striated pattern of microfibril bundles. The cells were digitally straightened and the upper half of the cell was analyzed for shape, fiber orientation (Figure 2C and 2D), and bundling (Figure 2E and 2H). Bundle spacings were consistently about 0.8 bundles/micron until a transition at 15 DPA after which the density of microfibril bundles was reduced to ~0.6 bundles/µm (Supplemental Figure 4). The non-parametric Dunn's test revealed a 6-14 DPA grouping and a 15-24 DPA grouping, with significant differences being found almost exclusively in pair-wise comparisons between the two groups (Supplemental Table 3).

The image analysis method could also detect transversely oriented bundles along the length of fibers (Figure 2F) and canted helical arrays (Figure 2G) that have been previously reported (Seagull, 1986). The helical arrays were not entirely stable along the length of the fibers and handedness-switching can occur (Seagull, 1986). The cell domains with microfibrils with a fixed handedness were usually large, but in rare instances an entire domain with switched handedness of ~100 µm could be clearly detected using the OrientJ fiber orientation quantification method (Figure 2G). We consider this an estimate of the lower limit of the domain length containing a switched handedness.

The presence of the fiber tip in an image and the biased orientation of the fibers on the slide enabled us to resolve left- and right-handed helical microfibril arrays (Figure 3). The fiber orientation method was applied to quantify the microfibril networks and fiber shapes throughout the 6-24 DPA interval. Images were collected from two different subcellular locations: at random distal fiber locations without a visible apex (Figure 3A, Supplemental Figure 2) and at apical zones that contained an intact fiber tip (Figure 3B, Supplemental Figure 2). Initial characterizations of microfibril angles were done by calculating the mean orientation angle of all ROIs within each cell and recording the mean orientation value for all cells in the dataset (Supplemental Table 4). At both subcellular locations, the mean orientations of the microfibrils per cell were dispersed but transversely oriented from 6-14 DPA (Supplemental table 1D-1G). At 15-16 DPA the orientations became more variable in both the apical domain and at distal random locations, and by 20 DPA the orientations shifted to a clearly biased toward a left-handed helical array (Figure 3C and 3D). The left-handed bias was not stable at later time points. The increased level of variability in mean fiber angle in the cells after 20 DPA (Figure 3E and 3F) reflected mixed populations of either a left- or right-handed dominant arrays in cells because a clear bimodal distribution of angles are observed when all ROIs are pooled and analyzed in aggregate at each DPA (Figure 3G and 3H). However, the angles of skew relative to the transverse axis were similar in right- and left-handed helical microfibrils (Figure 3I and 3J).

Tip morphology and fiber diameter control

Next, several morphological traits were measured from the same confocal images (Figure 4, Supplemental table 5). *G.h.* tapers to a mean diameter of ~8 µm (Stiff and Haigler, 2016), but the growth process is noisy with highly skewed distributions of tip geometries (Applequist, et al., 2001; Graham and Haigler, 2021; Stiff and Haigler, 2016; Yanagisawa, et al., 2022). In our dataset, the mean apex diameter usually fell below 10 µm and was variable within each DPA (Figure 4A). Bimodal distributions of apex diameters have been reported for *G.h.* at early developmental stages (Stiff and Haigler, 2016), and certainly, additional sampling would be required to enable reliable statistical analyses of apex curvature across this wide range of DPA. This variability in the minimum cell diameter in the apical domain was reflected in inconsistent morphologies of the fiber apex (Figure 4C, Supplemental 2B, Supplemental Figure 3). "Bulged" fibers with a localized swelling at the apex were frequently observed, as were fibers classified as "re-tapered" based on the assumption that these cells were re-establishing the tapering process from a bulged morphology, but it is possible that this population reflects distal swelling of a highly tapered cell. Aberrant tip morphologies were common across developmental time, as nearly half of the fiber tips deviated from the gradually tapered morphology that is often observed during the tapering process (Graham and Haigler, 2021; Stiff and Haigler, 2016; Yanagisawa, et al., 2022). The imperfect nature of cell diameter control was also reflected in an increased cell diameter at more proximal random locations compared to those in the apical region. The diameter at the proximal end of the fiber was statistically larger than that at the tip for all but 6, 9, and 22 DPA (Figure 4B). The microfibril patterns in swollen tips was highly variable (Supplemental Figure 2) and there was no clear pattern that might predict or explain the local shape defects from the imaging pipeline. Regions of local swelling were examined for differences in bundle spacing, but no extreme local variability was observed (Supplemental Figure 4).

Plausible biomechanical causes of apical swelling

Finite element modeling is an efficient computational tool to predict the types and spatial distributions of cell wall properties that are most critical to maintain normal cell shape during morphogenesis. Finite element analysis simplifies geometric or mechanical complexity by representing an object as a composite of elements with simpler geometries and properties. FE is well suited to problems in plant cell morphogenesis (Bidhendi and Geitmann, 2018) and has specifically been used to analyze a conserved tapering and cell diameter control mechanism in Arabidopsis leaf trichomes (Yanagisawa, et al., 2015) and cotton fibers (Yanagisawa, et al., 2022). Here we employed an anisotropic hyperelastic model—the Holzapfel-Gasser-Ogden model (Gasser, et al., 2006; Holzapfel, et al., 2000) similar to Yanagisawa et al., 2015, because it includes the orientation (θ) that we measured in the cell populations in Figure 3. Additional key parameters that potently influence cell shape are fiber stiffness (K_1), fiber dispersion (κ), the matrix modulus (E_m) (Yanagisawa et al., 2015). In the following simulations we analyzed combinations of variables to test for interactions among the variables in terms of simulated cell shape outputs.

First, the cells were considered to have uniform material properties. The fiber model was seen to axially deform within the flank region, showing primarily diffuse or mixed growth

dependent on the fiber bundle orientation (Figure 5B). As in a previous study, the cotton fiber was seen to globally swell as cellulose microfibrils become more axially oriented (Figure 5C, Supplemental Video 1). Fiber growth and tapering both rely on K_1, κ, E_m, and θ; variation in these parameters alters the aspect ratio and the global swelling of the growing cell (Figure 5D). An increase in θ or K_1 enables tapering and elongation, but an increase in κ hinders tapering and elongation. Softening of the matrix material also produces increased growth and tapering when there is a more transverse oriented fiber. However, changes of these parameters within a biologically relevant range do not create local bulging.

Next, to explain local bulging, the cell wall must be treated as if there were nonuniform properties from the tip to the flank (Figure 6A). Material gradients have been previously examined using finite element analyses in both isotropic elastic and anisotropic viscoelastic cell developmental models (Fayant, et al., 2010; Yanagisawa, et al., 2015). Cotton fibers early in development (<10 DPA) have been shown to contain gradients near the tip region in methyl-esterified homogalacturonan, xyloglucan, and cellulose (Stiff and Haigler, 2016). Based on the molecular gradients, we employed two types of mechanical gradients. Because of a higher degree of metyl-esterified homogalacturonan at the apex in hemisphere tips, the region near the apex was treated with a softer matrix modulus. Second, as cellulose content was reduced at the fiber apex, the K_1 parameter was also reduced. A gradient in both the matrix modulus and K_1 was able to produce slight apical swelling; the apical swelling was more dramatic when both gradients were used (Figure 6B). However, the degree of apical swelling was controlled by θ, K_1, and κ. Changes in local swelling with varied θ and κ were seen regardless of whether the gradient was just in E_m (Figure 6C) or in both E_m and K_1 (Figure 6D). Overall, characteristics that resist global swelling also resist local swelling.

Correlated fiber phenotypes and the expression dynamics of the cellulose biosynthesis network

We next wanted to integrate our fiber growth, wall thickness, and microfibril orientation phenotypes with additional published data on quantitative traits over a similar developmental window (Figure 7). Fiber cells modulate turgor pressure by reversibly gating symplastic continuity with the adjoining seed coat epidermis (Ruan, et al., 2004; Ruan, et al., 2001). A simple interpolation strategy was used based on the five datapoints in Ruan et al., 2001 to generate an estimate of the daily turgor pressure values (Ruan, et al., 2001), assuming that the transitions between measured time points were smooth. The cellulose, pectin, and hemicellulose levels at the same daily interval have been published (Swaminathan, et al., 2024). Here, the data were reanalyzed to test for significant differences in cell wall fraction content for both the mass of component per boll and the fraction of each component in the cell wall across developmental time (Supplemental Figure 1). These phenotypes were aggregated with the other informative phenotypes described above and Pearson's correlation analysis was performed among all possible pairs to group phenotypes that are temporally correlated and potentially related to one another (Figure 7A). Interestingly, the estimated relative growth rate, which is the most realistic for a diffuse growth mechanism, is most strongly correlated with the rapid initial decrease in the proportion of pectin (Supplemental Figure 1D). Interestingly, the pectin increase at 24 and 25 DPA matches the large increases in cellulose (Supplemental Figure 1A and 1C) and maintains its proportion at these time points, unlike hemicellulose (Supplemental Figure 1D,1F). The observed shift in microfibril angle at 16 DPA was broadly correlated with parameters that reflect transition

to secondary cell wall synthesis. The microfibril angle correlations were strongest with the cellulose amount and proportion (Figure 7A). The estimated turgor pressure profile was not correlated with any other parameter in our dataset.

In order to gain molecular knowledge about the genes that might mediate changes in microfibril patterning and cellulose accumulation, we probed a *G.h.* time series RNAseq dataset (Grover, et al., 2024) for known genes in a cellulose synthesis module that contain CESAs and a variety of other enzymes, structural, and cytoskeletal proteins (Gu and Rasmussen, 2022; Polko and Kieber, 2019). Cotton orthologs of known *Arabidopsis* genes were identified using inParanoid (Sonnhammer and Ostlund, 2015), and included: orthologs of COBRA (Benfey, et al., 1993; Roudier, et al., 2005; Schindelman, et al., 2001), Glycosyl Hydrolase 9/ KORRIGAN (Nicol, et al., 1998; Urbanowicz, et al., 2007), Cellulose synthase Interacting1 (CSI1), (Gu, et al., 2010) Companion of cellulose synthesis (CC1) (Kesten, et al., 2019), and Cellulose-Microtubule Uncoupling (CMU) (Liu, et al., 2016). The mean expression level in the normalized units of transcripts per million/kB (TPM) are summarized in Figure 7B and Supplemental Table 6. The expression groups, labeled T (transient peak), P (primary) and S (secondary), only partially conformed to an expected sub-functionalization of primary (e.g. CESA1,3,6) and secondary (e.g. CESA4,7,8) cellulose synthases(Tuttle, et al., 2015). For example, numerous CESA1 and CESA6 orthologs have transient peaks of maximal expression within the 6 to 15 DPA window. Along similar lines, and as reported previously for GhCESA4 (Kim, et al., 2011), a subset of predicted SCW CESA4, -7, and -8 orthologs are upregulated to very high expression levels after the transition to SCW synthesis (Figure 7B, class S). A proteomic analysis of CESA isoforms across the same developmental window validates that these SCW CESAs are clearly the most highly accumulated enzymes in the CESA family (Grover, et al., 2024). These expression data reflect a complex utilization of CESA orthologs and instances of homeolog-specific expression that does not reflect a simple model of strict subfunctionalization of primary and secondary wall CESAs.

However, there were numerous exceptions to this binary division of cellulose synthesis labor. As reported previously (MacMillan, et al., 2017), GhCESA8A homeologs are expressed at their highest level very early in development, and proteomic analyses confirm this expression profile at the protein level (Grover, et al., 2024). Conversely, predicted primary wall synthases GhCESA6B, GhCESA3C, and GhCESA4A homeologs had a maximum expression at 23 DPA. Interestingly, both GhCESA3B homeologs had a transient high level of expression peak centered on 15 DPA (class T). The Dt homeologs of GhCESA3A, GhCESA3C, and GhCESA1A had broad expression patterns with peaks at ~15 and ~22 DPA (class S). GhCESA1-A-At and GhCESA3-A-At were part of a loosely organized group (Figure 7B, bottom) that had a more uniform expression across most of the 6 to 24 DPA window.

The expression groups in Figure 7 provides clues about which subsets of additional cellulose biosynthesis genes might work together over time to orchestrate fiber wall assembly. The most striking temporal variabilities were in the GhGH9/KORRIGAN and COBRA and COBRA-like orthologs. The cotton orthologs GhCOB-At/Dt, which are most closely related to *Arabidopsis* COBRA, were the most highly expressed at early stages, with a progressively decreasing expression across DPA. Both COBL4-A homeologs, COBL4-D-At , and COBL1-Dt were strongly and transiently induced during the 13-15 DPA interval. There were 11 COBL4/6/7 genes with a clear induction at or near the transition to SCW synthesis that placed them the “S” expression group. The group was dominated by the 8 COBL4/IRX6 orthologs, including a massive induction from GhCOBL4-E-At from undetectable at 6 DPA to over 400 TPM at 22

DPA (Figure 7B, Supplemental Table 6). All GH9 orthologs had a progressively increasing expression pattern and fell into the "S" group. This does not imply exclusive SCW function because the GhGH9A1-A-At/Dt homeologs were both expressed above 100 TPM early, and have extremely high expression levels above 600 by 19 DPA (Figure 7B, Supplemental Table 6). The GH9A1-B-At/Dt pair has a similar profile but their baseline expression is ~10 TPM at early stages. A proteomic analysis of protein abundance across the same developmental timeline indicates that these GH9 orthologs mentioned above are the predominant proteins in the fiber cells (Lee, unpublished). The CSI, CC, and CMU genes displayed less temporal variability compared to the GH9 and COBRA orthologs (Figure 7, Supplemental Table 6). Based on expression levels we predict the key genes of each type to be: for CSI1; GhCSI1-A-At/Dt; CC genes, both homeologs for CC1E, F and CC3B, CC1A-Dt, CC1C-At; for CMU, both homeologs for CMU1-B, CMU2-A, and CMU3-A.

DISCUSSION

This paper reveals previously unrecognized temporal variability and in growth rate, microfibril network organization, and cell shape control during fiber development. The data provide novel insights into the biomechanical control of fiber elongation, cell diameter control, and wall patterning that likely determines the degree of twist upon desiccation. Therefore, the work here provides a foundational dataset to predict systems of genes and cellular functions that are likely relevant to cotton improvement. The prospects of using molecular genetics to engineer cotton fiber phenotypes show promise. The combined use of detailed biochemical profiling of fiber cell wall composition across development (Avci, et al., 2013; Pettolino, et al., 2022), computational and biomechanical analyses of cell wall function (Keynia, et al., 2022; Yanagisawa, et al., 2015; Yanagisawa, et al., 2022; Zhang, et al., 2021), and time-series multivariate analyses of cellular dynamics (Sambade, et al., 2014; Yanagisawa, et al., 2015) are providing unprecedented insights into how fiber cells pattern growth and the final shape of the desiccated cell. The major remaining challenge is to identify the key genes and control modules that can be used to specify fiber traits through cotton transformation experiments. Integrating knowledge from model systems that reveal a conserved control mechanism with temporally resolved multi-omic profiling of cotton fibers provides an efficient mechanism for gene discovery, hypothesis testing, and proof of concept for the rational engineering of cotton fiber traits. New insights into the timelines, potential cellular controls, and biomechanical processes that underlie fiber traits are discussed below.

Growth rate reduction precedes secondary cell wall synthesis

Growth rate variability during fiber development is poorly understood. Within a limited windows of fiber development, the length changes at the whole cell scale appear somewhat linear. Linear length increases would be expected for tip-growing cells like root hairs, that propagate self-similar shapes by selectively adding new wall material and restricting growth to the extreme apex. The possibility that fibers employ combinations of tip- and diffuse-growth

mechanisms and an apical zone of active growth has been widely discussed (Qin and Zhu, 2011; Stiff and Haigler, 2016; Yu, et al., 2019).

The length change profile from growth-chamber-grown plants (Figure 1D) closely matched that of field-grown plants (Schubert, et al., 1973), with maximal length increases occurring at ~10 or 11 DPA. Previous experimental data support a predominant diffuse growth mechanism for cotton fibers (Graham and Haigler, 2021; Ryser, 1977; Seagull, 1993; Szymanski and Staiger, 2018; Tiwari and Wilkins, 1995; Yanagisawa, et al., 2022). The relative growth rates, accounting for length, are maximal from 5-7 DPA and progressively decreased until relative growth was minimal after 20 DPA (Figure 1D). Cell wall thickness gradients within cells can explain cellular-scale growth behaviors (Yanagisawa, et al., 2015), and it is generally assumed in the cotton fiber literature that growth rate dynamics are linked to the transition to secondary cell wall thickness and a thicker, tougher cell wall. The SCW transition usually begins at ~16 DPA (Figure 1F), and in a parallel RNAseq analysis a suite of SCW, CESA were transcriptionally activated from ~9 -14 DPA (Grover, et al., 2024). Cell wall analyses of the same material detected a significant increase in cellulose at ~17 DPA (Supplemental Figure 1). Clearly, fiber elongation rates, independent of the method used to calculate them, decrease well before a thicker SCW is detected (Figure 1D). Relative growth rates estimated from length data in the 2-4 DPA window of *G.h.* development are 75-110%/day (Graham and Haigler, 2021). The increased cell wall thickness in 6 DPA fibers (Figure 1E) could reflect an extensive remodeling of cell wall matrix, and an increased stiffness could partially explain a decreased growth rate from the initial tapering to elongation phases. Mechanical modeling of trichoblast growth in *Arabidopsis* (Yanagisawa, et al., 2015) predict that complex interactions among cell wall thickness, matrix stiffness, and turgor pressure modulation affect growth rate. Cotton fiber glycome profiling at high temporal resolution (Avci, et al., 2013) (Swaminathan, et al., 2024) and analyses of turgor pressure variability during the fiber elongation phase (Ruan, et al., 2001) suggest that each of these parameters modulate growth rate prior to SCW synthesis. Factors such as expansins and XETs are often invoked as molecules that can decrease wall stiffness and promote growth (Cosgrove, 2000; Ruan, et al., 2001), but questions remain about their mode of action (Cosgrove, 2024; Fang, et al., 2018).

Cell diameter instability at the apex and cell flanks

The cortical microtubule-CESA guidance-aligned microfibril synthesis module is a cell signaling and biomechanical control system that programs morphological complexity across species lines and broad spatial scales. A major challenge is to determine which microtubule behaviors orchestrate shape change at what subcellular locales (Belteton, et al., 2021; Crowell, et al., 2011; Elliott and Shaw, 2018). The complexity of the problem is greatly reduced in trichoblasts. A highly organized transverse array along the cell flanks and an apical zone with reduced microtubule density mediate cell elongation and tapering, respectively (Yanagisawa, et al., 2015; Yanagisawa, et al., 2022).

As observed previously with the cortical microtubule array (Seagull, 1986; Seagull, 1992), our microfibril imaging and analysis pipeline detected bundle arrays with a transverse bias that persisted until 14 DPA; however, the alignment was variable (Figure 3C-3G). Cell diameter is initially set at the apex during a tapering process that is completed by ~2 DPA (Yanagisawa, et al., 2022), but we detected clear evidence for cell swelling during fiber elongation. The cell diameter near the apex was consistently less than that in random locations

near the distal end. We hypothesize that because of the sensitivity of cell swelling to fiber organization; variability in bundle organization causes progressive swelling during development. We were not able to detect significant differences in the microfibril bundle spacing in swollen domains of the cell (Supplementary Figure 4).

However, global swelling (Figure 5) can occur within the range of mean fiber angles observed during fiber elongation (Figure 3G-H), so local variability in fiber angle could cause differences in swelling. Our mechanical modeling results match previous models (Yanagisawa, et al., 2015; Yanagisawa, et al., 2022), predicting that minor deviations of fiber orientation off the transverse axis enable radial swelling (Figure 5). The anisotropic properties control the relationship between fiber tapering and global swelling for a cell with uniform mechanical properties. Increases in K_1 (for the θ values studied here) and θ increase the transverse stiffness to a greater degree than axial stiffness. Decreases in κ align fibers more in the mean direction and decrease material isotropy. All three of these trends favoring anisotropy increase tapering and cell elongation. From a simplified perspective, if the cell wall resists radial expansion and allows axial growth through microfibril orientation, the cell should taper if it has uniform material properties.

Tip morphology was also highly variable in the cell apex (Figure 4). Cortical microtubules align with the magnitudes and directions of cell wall tensile forces (Belteton, et al., 2021; Green and King, 1966; Hamant, et al., 2008; Oda, 2015; Williamson, 1990). Stress patterns are strongly affected by the cell geometry (Kierzkowski and Routier-Kierzkowska, 2019), and a spatially resolved force sensing mechanism may play a major role in patterning microtubules and the cell wall in trichoblasts. Variability in the signaling proteins and cellular machineries that mediate wall stress sensing and cell wall patterning could contribute to local cell swelling and its remediation in growing *G.h.* cotton fibers.

To test the hypotheses of the roles of fiber organization in aberrant tip geometries, we performed finite element analyses of growing cells. For a cell with uniform mechanical properties, tip swelling did not occur regardless of the value of mechanical properties (Figure 5). This indicates that the geometry of the fiber alone is not enough to induce tip swelling. Tip swelling occurs when there are material property gradients from the tip to the flank, and the degree of tip swelling is then controlled by the degree of the gradient and by material anisotropy. Gradients in the fiber or matrix stiffness (K_1 and/or E_m), with softer material at the tip, induce tip swelling. These gradients can be controlled through the local deposition of material. While E_m can be linked to physical properties of the pectin matrix, K_1 does not easily relate to cellulose fiber properties. For the simplest fiber composite models, the contribution of fiber reinforcement to the composite modulus depends on both the fiber stiffness and the fiber fraction. As the anisotropic model used in this work provides a more complex understanding of fiber stiffness, there remains a disconnect between the parameter K_1 and cellulose fiber properties. However, it can be considered as a kind of anisotropic modulus, with increases in K_1 increasing the contribution of the anisotropic free energy similarly to how E_m increases the contribution of the isotropic free energy. Gradients in either the isotropic modulus of the matrix or this anisotropic modulus of the fibers alter the local stiffness of the expanding cell and can enable tip swelling. The degree of bulging depends on the axial-transverse anisotropy. If the softer regions strongly resist radial expansion through increased K_1, increased θ, or decreased κ, fiber elongation can still occur without local bulging, even in the presence of material gradients. Increased amounts of methyl-esterified homogalacturonan and reduced amounts of crystalline cellulose were seen at the apex in the tapered *G.b.*, while similar gradients occurred in the hemispherical *G.h* but not

the tapered *G.h.* (Stiff and Haigler, 2016). The similarity in molecular patterning but differences in geometry might be explained by differences in fiber organization or mechanical properties in *G.h.* and *G.b.*

Developmental transitions and instabilities of cellular scale microfibril bundle networks

At 15 DPA, microfibril ordering becomes more variable within and between cells (Figure 3C-3H). During this transition, the microfibril array transitions toward a bias of left-handed helical arrangement at cellular scales. This timing and pattern correlates with a reported transition to a spiraled pattern of microtubules (Seagull, 1986). Under our growth conditions, the timing of this transition correlates with a massive rewiring of the transcriptome that includes the transcriptional activations of subsets of SCW CESAs (Grover, et al., 2024; Lee, unpublished; Swaminathan, et al., 2024). In *Arabidopsis* leaf trichomes, the cortical microtubule array similarly transitions from transverse to a longitudinal/helical array (Basu, et al., 2005; Zhang, et al., 2005) after the overall shape of the cell is determined at stage 4 and the cell enters a phase of rapid diffuse growth (stage 5) that is rather isotropic in nature (Yanagisawa, et al., 2015). During stage 5, a clear bias toward a left-handed cortical is detected (Keynia, et al., 2022; Sambade, et al., 2014). This left-handed bias in microtubules patterns cellulose fibers in the wall, because upon desiccation the cell twists with the same bias in handedness (Keynia, et al., 2022).

The left-handed bias in bundle orientation may reflect the proposed existence of a specific "winding" layer of cellulose in the developing fiber. However, the left-handed bias is unstable, and after 20 DPA, mixed populations of left- and right-handed microfibril bundles occur within and between cells (Figure 3C-3H). It is not known what governs the transitions between transverse, left-, and right-handed microtubule arrays; however genetic evidence in *Arabidopsis* and cotton point to the involvement of tubulin subunits, microtubule-associated proteins, and actin filament nucleators (Buschmann and Lloyd, 2008). Perhaps the initial transition from transverse to helical reflects the attenuation of a cell wall stress-dependent patterning mechanism that maintains transverse arrays and an apical microtubule-depletion zone, to some another mechanism in which microtubule structure and cell geometry interact to generate interconvertible spiraled patterns.

MATERIALS AND METHODS

Growth conditions

Gossypium hirsutum cv. TM1 plants were grown in Classic 2000 pots (Nursery Supplies, Inc) in a growth chamber under a 16/8 day/night cycle at 28 °C in soil (Sungro Professional Growing Mix), perlite (Therm-O-Rock), bark (OrchidSupply.com), and crushed quartzite (Cherry Stone Grit) mixed at a 4:2:2:1 volume ratio. Plants were fertilized at least weekly to saturation with Miracle Gro. Flowers were tagged on the day of anthesis (Day 0) and characterized by their days post anthesis (DPA).

Cell wall thickness: published data aggregation and measurements

The methodology employed to gather cell wall thickness data encompassed several rigorous steps. Initially, a comprehensive literature review was conducted to source relevant information. Subsequently, Transmission Electron Microscopy (TEM) images were gathered and subjected to meticulous analysis. The measurement of cell wall thickness was executed utilizing ImageJ, a widely recognized image analysis software. To ensure the robustness of the dataset, outliers were identified and eliminated utilizing an 85 percent prediction interval. This statistical approach aided in refining the dataset and enhancing its reliability. Finally, the visualization of the refined data and the generation of conclusive graphs were accomplished through the utilization of R, a statistical programming language. This methodological framework ensured the accuracy and integrity of the collected cell wall thickness data, thereby facilitating comprehensive analysis and interpretation

Fiber length measurements and statistical analyses

Whole cotton bolls were excised from the plant on the desired DPA, and each locule was isolated from the boll and placed in 1% v/v Nonidet-40 at 80 °C for 15 minutes for locules at 5-14 DPA and 20 minutes for locules at 15-25 DPA. Fibers were rinsed with 10 mM PBS (pH7) and then gently vortexed in 0.025 M HCl for one minute to enable fiber detangling (Stiff and Haigler, 2016). The 0.025 M HCl treatment did not affect the distribution of banded microfibrils along the length of the cells. Seeds were rinsed again with PBS buffer and then stored in PBS and 0.01% thimerosal at 4 °C until use. Mean maximal fiber length measurements were acquired by placing individual seeds on a glass slide, fanning the fibers into a halo around the seed with a stream of buffer, and then manually aligning the fibers parallel to the long axis of the seed. Images of the fibers were collected using an iPhone dual 12MP camera, and the mean maximum fiber length was measured (inset at 24DPA in Figure 1B) using Fiji for three separate seeds in three different locules of three different bolls for a total of nine measurements. To compare cell diameter in the apical domain to those measured in more distal random locations the minimum fiber diameter of each cell was measured. The distributions of values were tested for normalcy using the Shapiro-Wilk test. The Mann-Whitney U test was used in cases in which a dataset was not normally distributed, otherwise the Student's t-test was used. The number of individuals in each group is defined by the number of high quality images for each DPA and each subcellular location. Tip radius of curvature and local fiber diameter values were obtained from 10 or more cells at all DPA except for 16 and 24 DPA, which had 9 and 8 cells, respectively. Diameter at distal locations was measured from at least 15 cells at all DPA (Supplemental Table 2).

Cellulose staining and confocal microscopy

To prepare the fibers for confocal imaging, individual seeds were first removed from storage and placed in a petri dish. 10 mM PBS buffer was slowly poured over the seed to fan out the fibers in a halo, and the seed was bisected radially and then longitudinally to reduce fiber density. The chalazal halves were used for staining and imaging. The two halves of the chalaza were placed in 0.5% (w/v) calcofluor white for 10 minutes for staining. Each half was then placed on a glass slide, fibers were fanned out using PBS buffer to create a single plane of fibers, and then they were dissected from the seed and carefully covered with a glass cover slip to minimize crushing the fiber cells. Samples were mounted on an inverted spinning disc confocal microscope (Zeiss

Observer.Z1) and imaged using a water immersion lens (63x, 1.2NA, Zeiss) and a Prime 95B sCMOS camera (Photometrics) linked with the Slidebook software (Intelligent Imaging Innovation). Z-stacks of fibers were collected at 0.3 µm intervals using a 405 nm UV laser for excitation. Fiber cells were judged as acceptable for quantification if the cell retained its round shape based on focusing in Z, it did not cross another fiber cell, and the cell lacked artifactual punctate fluorescence or local creases. Fifteen or more images were captured for bolls aged 6-24 DPA at random locations along the length of fibers, and ten or more images of apical fiber domains were collected that had an intact tip (Supplementary Figure 2). A montage function was used for image acquisition when isolated fibers were close to the cover slip in more than one field of view.

Image processing and analysis

All Images were processed for analysis using Fiji (Schindelin, et al., 2012). Because of the fiber alignment protocol, most fibers were aligned with the tips oriented in a single direction. The image stacks were transformed about the horizonal axis to correct for an image inversion at the camera, and the slice keeper tool was used to select the images that captured half of the cell volume closest to the cover slip. Brightness and contrast of the images were adjusted and image stacks were rotated slightly so the tip was pointing to the right side of the image. The straightening tool was used to artificially generate a straight fiber, and finally the images consisted of projected maximum intensity. Image analysis was performed using a custom-built macro that prompted the user to define the fiber width at the narrowest region of the fiber, the length of the fiber, and a circle at the tip of the fiber to measure the radius of curvature or diameter at the apex. The macro then generated a sequence of square ROI's with measured lengths that were two-thirds that of the minimum diameter and one circular ROI with a radius two-thirds that of the radius of curvature at the fiber tip for images including tips (Supplemental Figure 2C). Using these ROI, the macro generated a .csv file including: fiber length, minimum diameter, ROC at tip, and area of the ROI, and for each ROI, skewness, kurtosis, raw integrated density, and normalized integrated density. Finally, using the OrientationJ plugin the orientation of cellulose microfibrils (Figure 2A) and the coherency of the orientation measurements were collected. We failed to detect any developmental variability in the coherency of the microfibril bundle network. Angles were defined with 90 degrees being transverse to the long axis of the cell. To quantify the microfibril angle changes relative to 90 degrees over developmental time, all mean angles of all ROIs were calculated as the absolute value of the deviation from 90 degrees. The allowed the angle deviations of left-handed and right-handed helical arrays that occurred after 15 DPA to be aggregated and quantified over time. To measure bundle spacing, a five-pixel wide line-scan was performed in Fiji along the midline shank. The gray values and their position along the line were exported and then analyzed using a custom Python script that applied the prominence method to distinguish local maxima by applying a 10% prominence threshold. Local maxima were interpreted as a microfibril bundle, and the number of bundles per 10 microns was measured by finding the distance between the initial and final peak and dividing this by the number of bundles along the line-scan.

Fiber growth rate calculations

We employed a nonlinear least squares method to fit a logistic growth curve to mean maximum fiber length data spanning from 5 to 24 DPA. The logistic growth model given by the following equation was utilized to describe the growth trajectory of the fibers:

$$L(t) = \frac{L_{max}}{1 + e^{-k(t-t_0)}}$$

where $L(t)$ represents the fiber length at time *t*, L_{max} is the maximum attainable fiber length, *k* is the growth rate parameter, and t_0 is the inflection point indicating the onset of rapid growth. By fitting the observed fiber length data to this model, we obtained the parameters, $L_{max}, k\ , t_0$. Subsequently, derivatives of the fitted logistic function were computed to obtain the growth rate over the time period. The relative growth rate is further calculated by dividing the growth rate by the fiber length at each DPA (Figure 1D).

Statistical analyses of cell wall composition from 6 to 24 DPA

Alcohol-insoluble cell wall was extracted from 6 to 25 DPA bolls in triplicates and, further, the pectin and hemicellulose polysaccharide fractions were extracted sequentially as described previously (Avci et al. 2012; Zabotina et al. 2012). In brief, using a sharp razor blade, fibers were separated from the seeds, ground to a fine powder in liquid nitrogen, and the CW was extracted by using organic solvents. The pectin and hemicellulose polysaccharides were extracted sequentially by using 50 mM CDTA:50 mM ammonium oxalate (1:1) buffer (*v*:*v*) and 4 M KOH, respectively. The extracts were dialyzed, dried by lyophilization, and weighed. The final pellet remaining after hemicellulose extraction is defined as the cellulose (mixture of both amorphous and crystalline celluloses), which was also dried and weighed. The three replicates at each DPA were subjected to statistical analysis using R Studio software. The data were initially tested for significance by analysis of variance (ANOVA) and subsequently Fisher's protected least significant difference (LSD) test value was used to compare treatment means at $p < 0.05$.

Finite element analysis of cotton fiber development

Finite element analysis (FE) was performed using ABAQUS 2021 (Dassault Systemes SIMULIA). The model used to simulate cotton fiber growth was based on previous FE of single cell systems, namely *Arabidopsis* trichomes—another cell which grows by a diffuse mechanism (Yanagisawa, et al., 2015). Cell growth was modeled through an iterative process using custom python scripts integrated with ABAQUS (Fayant, et al., 2010). In the first step, the cell was drawn as a 2D line structure that was rotated 360° to form a cylindrical shape with a hemispherical cap (Figure 5A). The initial radius of the hemisphere and the cylinder was set to 3 µm, and the height of the cylinder was 20 µm. Then, the cell was pressurized with an internal pressure of 0.2 MPa or 0.7 MPa, based on previous measurements of turgor pressure in developing cotton fibers (Ruan, et al., 2001). Then the coordinates of the deformed cell were extracted from the nodes along the initial drawn line. These coordinates were used to draw the line that was rotated in the subsequent growth step, and the process was repeated for 25 growth steps.

The cotton fiber was modeled with an isotropic region at the tip. While the tip region contains cellulose microfibrils, there is a region of microtubule depletion (Yanagisawa, et al., 2022). As microtubules help in orienting cellulose microfibrils (Paredez, et al., 2006), microtubule absence reduces cellulose microfibril order. Previous experimental work related the size of the microtubule depletion zone (MDZ) with the radius of curvature of the tip region (Yanagisawa, et al., 2022):

$$P = 1.3\,R + 1.7$$

where P is the perimeter of the MDZ (or arc length of the 2D circle) and R is the radius of curvature of the tip. In our simulations, we delineate the isotropic region with a transverse plane located a given distance from the fiber apex (h_{TIZ}). This distance can be defined geometrically using the following equation:

$$h_{TIZ} = R - R * \sin(\psi)$$

where ψ is defined by the perimeter and radius of curvature.

$$2 * \psi + \theta = \pi$$

$$\psi = \frac{\left(\pi - \frac{P}{R}\right)}{2}$$

The initial h_{TIZ} is set at 1.21 µm, based on the radius of curvature of 3 µm. In subsequent growth steps, h_{TIZ} is calculated using the radius of curvature from the deformed geometry.

The cotton fiber was treated following the fiber-reinforced Holzapfel-Gasser-Ogden (HGO) model(Gasser, et al., 2006; Holzapfel, et al., 2000), an anisotropic hyperelastic material model. The model considers the isotropic and anisotropic behavior as two additive terms. The HGO model is defined by the matrix modulus (E_m), a parameter related to fiber stiffness (K_1), a parameter related to the stiffening of the fibers (K_2), and the alignment of fiber angles (κ). A κ of 0.33 represents isotropic fiber alignment, and κ of 0 represents fully aligned fibers. In our model, we treated the material as incompressible and assumed a Poisson's ratio of 0.5. The K_1 parameter does not have a direct physical meaning, but increases in its value represent increases in the strain energy of the anisotropic term as a function of extension. In the original HGO model of arteries, the K_2 parameter was used to describe fibers which do not initially bear load but bear load upon material extension. In our case, we have kept the value of K_2 at unity. The isotropic region is modeled using κ = 0.33 to represent isotropic cellulose microfibril orientation. The mean fiber orientation is defined in ABAQUS. Viscoelastic properties were defined by a 12.5% decrease from initial to infinite modulus and a relaxation time of 6.88 s (Yanagisawa, et al., 2022).

Two boundary conditions were defined. The first prevented the bottommost circular edge of the flank from displacing in the axial direction. The second allowed only axial displacement of the tip apex, preventing fiber bending. The free mesh was defined with a quad-dominated element shape and a seed size of 0.25 µm. Shell elements (S4R) were used. The load pattern was defined by a tabular amplitude with 0% of the applied load at 0 seconds, and 100% of the load

applied by 0.005 s. This loading pattern prevented convergence errors in the FE calculation, while still applying the full load over a much shorter time than the relaxation time.

The cell geometry was evaluated through the normalized aspect ratio, and the inverse of the normalized radius of curvature of the isotropic zone. The radius of curvature of the isotropic zone was determined by fitting a circle to the data points with $y > (y_{max} - h_{TIZ})$, where y_{max} is the deformed tip apex position and h_{TIZ} is defined before deformation.

Models were also defined with material gradients from the tip towards the flank. Three transverse planes were drawn at a constant separation from the h_{TIZ} (2 µm). The gradient was defined by three terms: the tip modulus, the flank modulus, and the slice size. The modulus of each section was calculated through a power function:

$$E_i = E_{m,tip}\left[\left(\frac{E_{m,flank}}{E_{m,tip}}\right)^{\frac{1}{n+1}}\right]^i$$

where E_i is the modulus for a layer out of *n* layers with the index *i* = 0 corresponding to the tip and progressing towards the flank. $E_{m,flank}$ was set at 400 MPa; $E_{m,tip}$, at 100 MPa; *n*, at 3.

ACKNOWLEDGEMENTS

The authors would like to thank Dr. Thomas Siegmund and Dr. Anastasia Desyatova for helpful discussions on finite element analysis. Artificial Intelligence (ChatGPT) was used in the development of code for data analysis and producing graphical elements. This research was supported by the National Science Foundation (NSF) Grant No. 2148122 to C.S.D. and D.B.S. and by Grant No. 1951819 to, J.F.W, O.Z., J.X, and D.B.S.

CONFLICTS OF INTEREST

The authors have no conflicts of interest to declare.

FIGURES

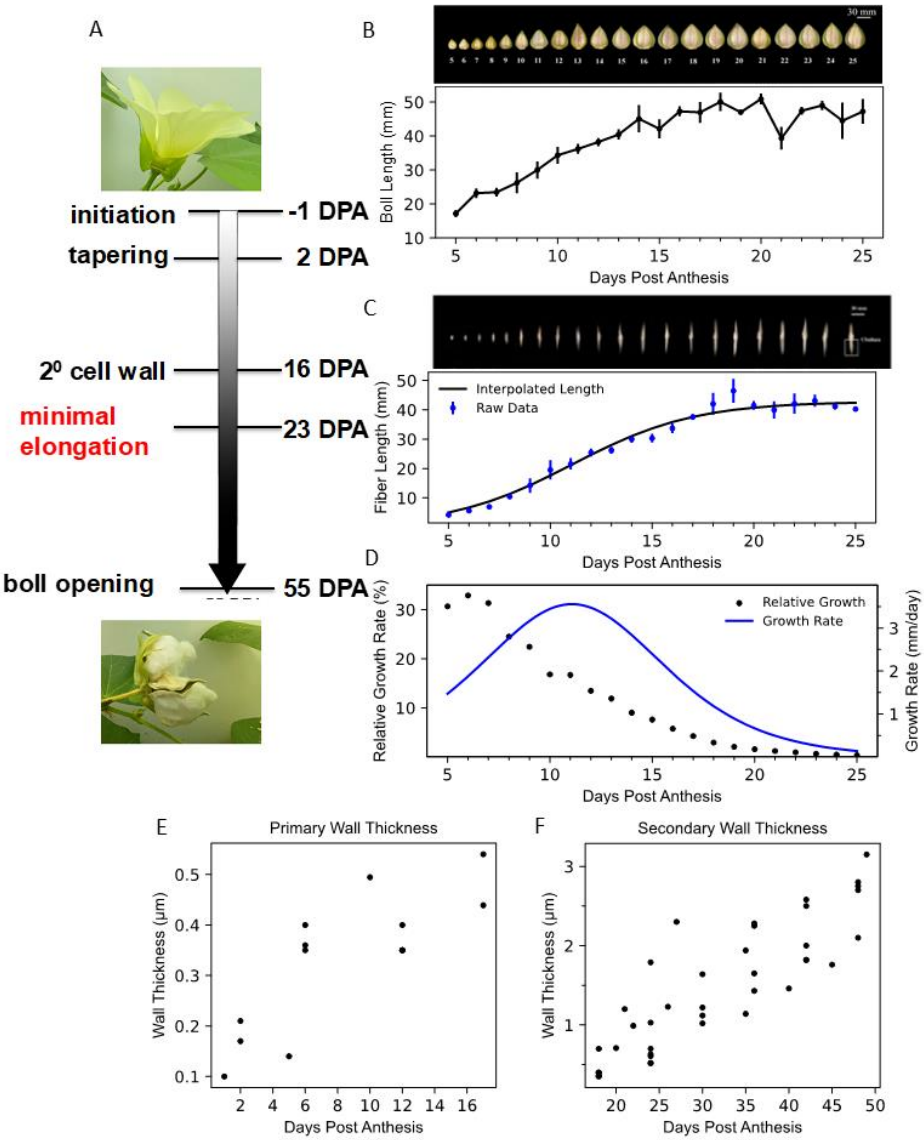

Figure 1: A high temporal resolution analysis of *G. hirsutum* fiber development.
(A) Developmental stages of cotton fiber growth, where the white gradient details when fibers are elongating.
(B) Daily sampling of cotton bolls and boll lengths (n=3) from 5-25 DPA.
(C) Daily sampling of ovules (n=9 for each day) used for measuring the mean maximum fiber length of combed fibers (box at 24 DPA). Mean and standard deviation of the fibers is shown below fitted with a logistic regression curve.
(D) The growth rate of fibers was determined from the first derivative of the logistic regression (blue line), and then dividing the rate by mean length of the fibers was performed to measure the relative growth the at daily intervals (black dots).
(E) Thickness of the cell wall measured during primary growth and
(F) during secondary wall thickening.

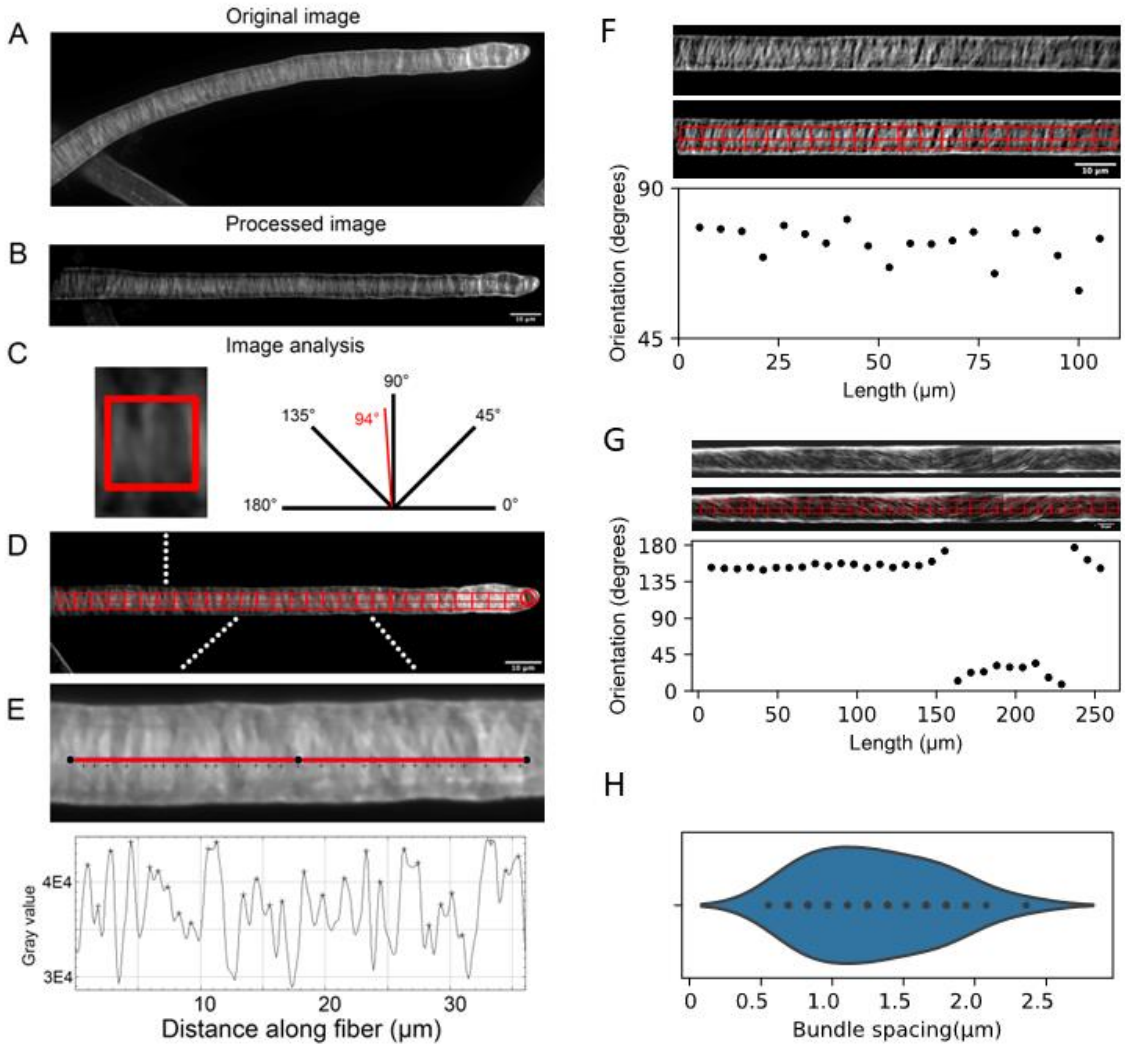

Figure 2: Image processing pipeline for microfibril and cell shape quantification.
(A) An example maximum projection of ~1/2 of the cell volume observed following montaged confocal microscopy of calcofluor-stained cotton fibers.
(B) Images were processed to digitally straighten the fiber and subtract background.
(C) Schematic diagram defining the angles measured to describe microfibril orientation, with an example from the indicated ROI in (D).
(D) The location of the fiber apex, radius of curvature at the tip, and the minimum cell diameter were used to generate an array of ROIs to quantify cell geometry and mean fiber orientation angles.
(E) inset of the region outlined in (D) where a line-scan of the intensity profile was used to identify the location of microfibril bundles (individual crosses beneath the line scan).
(F) Representative 13 DPA fiber
(G) Rare 21 DPA fiber the contains the boundaries in which the handedness of the bundles switches from right to left to right. The measured angles using OrientJ are shown below.
(H) Distribution of bundle spacing measurements from the line scan generated in (E).

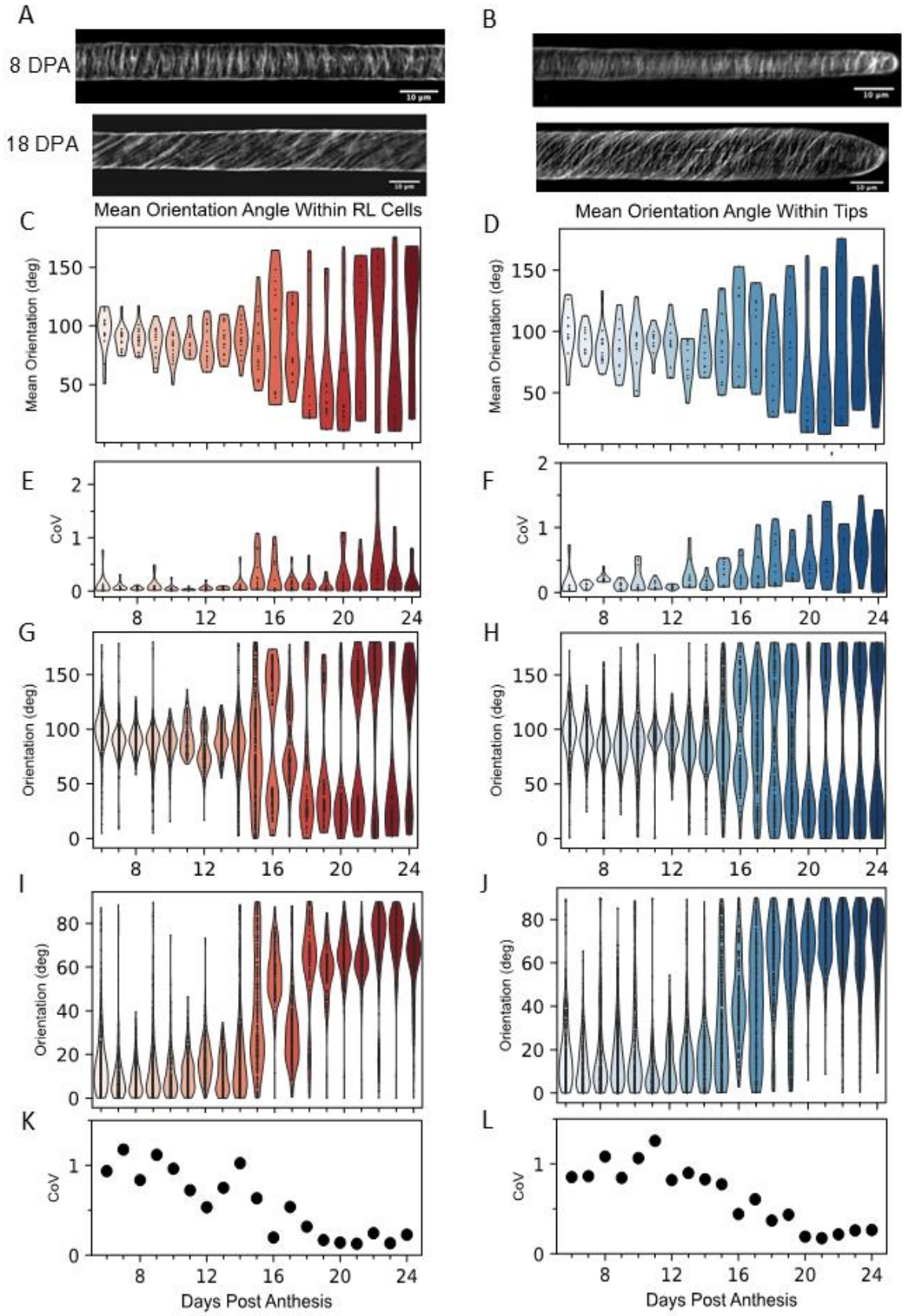
A
B
8 DPA
18 DPA
Mean Orientation Angle Within RL Cells
Mean Orientation Angle Within Tips
C
D
E
F
G
H
I
J
K
L
Mean Orientation (deg)
CoV
Orientation (deg)
Days Post Anthesis

Figure 3: Microfibril organization as function of subcellular location and developmental time.
(A) Example images of 8- and 18-days post anthesis (DPA) fibers stained with calcafluor white obtained from random locations along the length of fibers or
(B) at the fiber tip.
(C) Distribution of mean microfibril bundle angles of cells at random locations from 6 to 24 DPA.
(D) Distribution of mean microfibril bundle angles of cells in apical domains from 6 to 24 DPA.
(E) Coefficient of variation of angle distributions at random locations from 6 to 24 DPA.
(F) Coefficient of variation of angle distributions in apical domains from 6 to 24 DPA.
(G) Distribution of mean microfibril bundle angles of all individual ROIs measured at random locations from 6 to 24 DPA.
(H) Distribution of mean microfibril bundle angles of all individual ROIs measured in apical domains from 6 to 24 DPA.
(I) Distributions of mean microfibril bundle angle deviations from transverse measured at random locations from 6 to 24 DPA.
(J) Distributions of mean microfibril bundle angle deviations from transverse measured in apical domains from 6 to 24 DPA.
(K) Coefficient of variation of angle distributions of mean microfibril bundle angle deviations from transverse measured at random locations from 6 to 24 DPA.
(L) Coefficient of variation of angle distributions of mean microfibril bundle angle deviations from transverse measured in apical domains from 6 to 24 DPA.

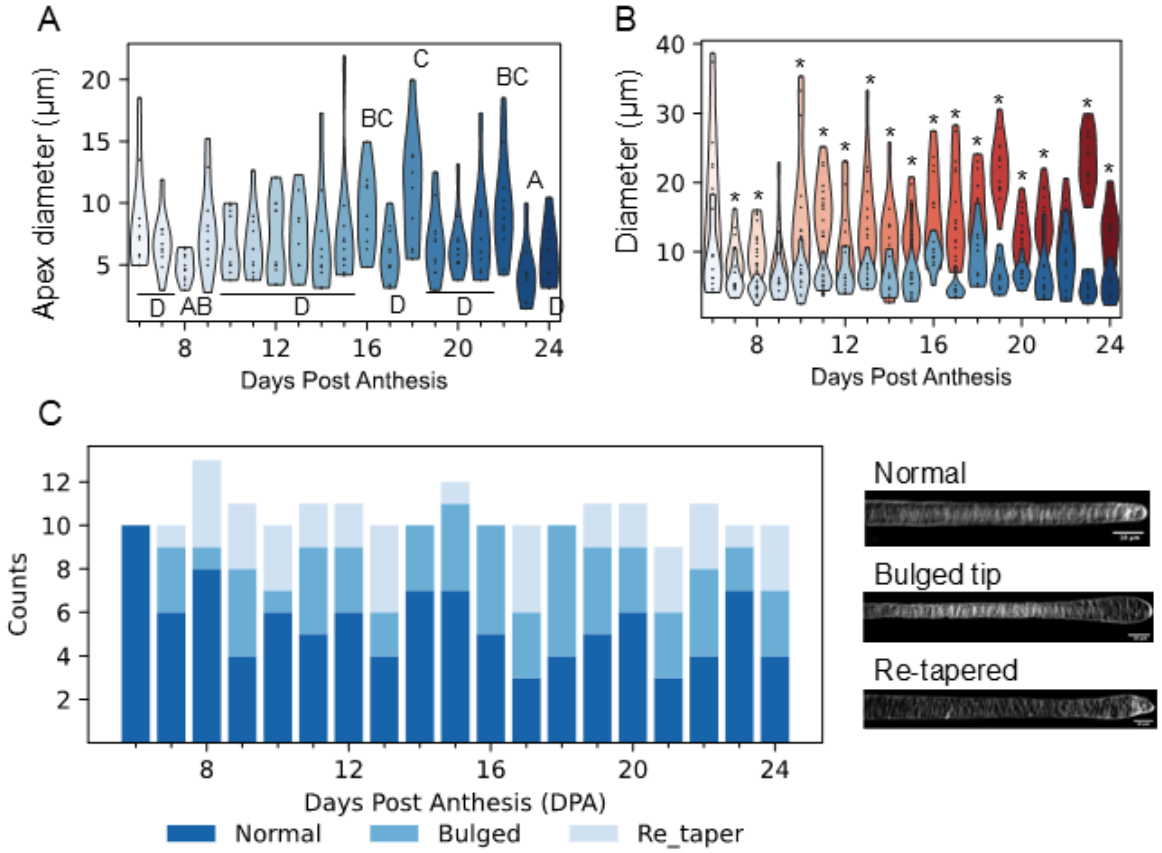

Figure 4: Variability in cell diameter as a function of location and development.
(A) Cell diameter variability in the apical domain of growing fiber cells.
(B) Comparisons of cell diameter in the apical domain compared with those measured at distal locations (red). Asterisks indicate significant differences between the two subcellular locales.
(C) Alternative tip morphologies of the fiber apex as a function of DPA. Tip morphologies were classified as normal, bulged, or re-tapered. Color coded key is shown below panel C.

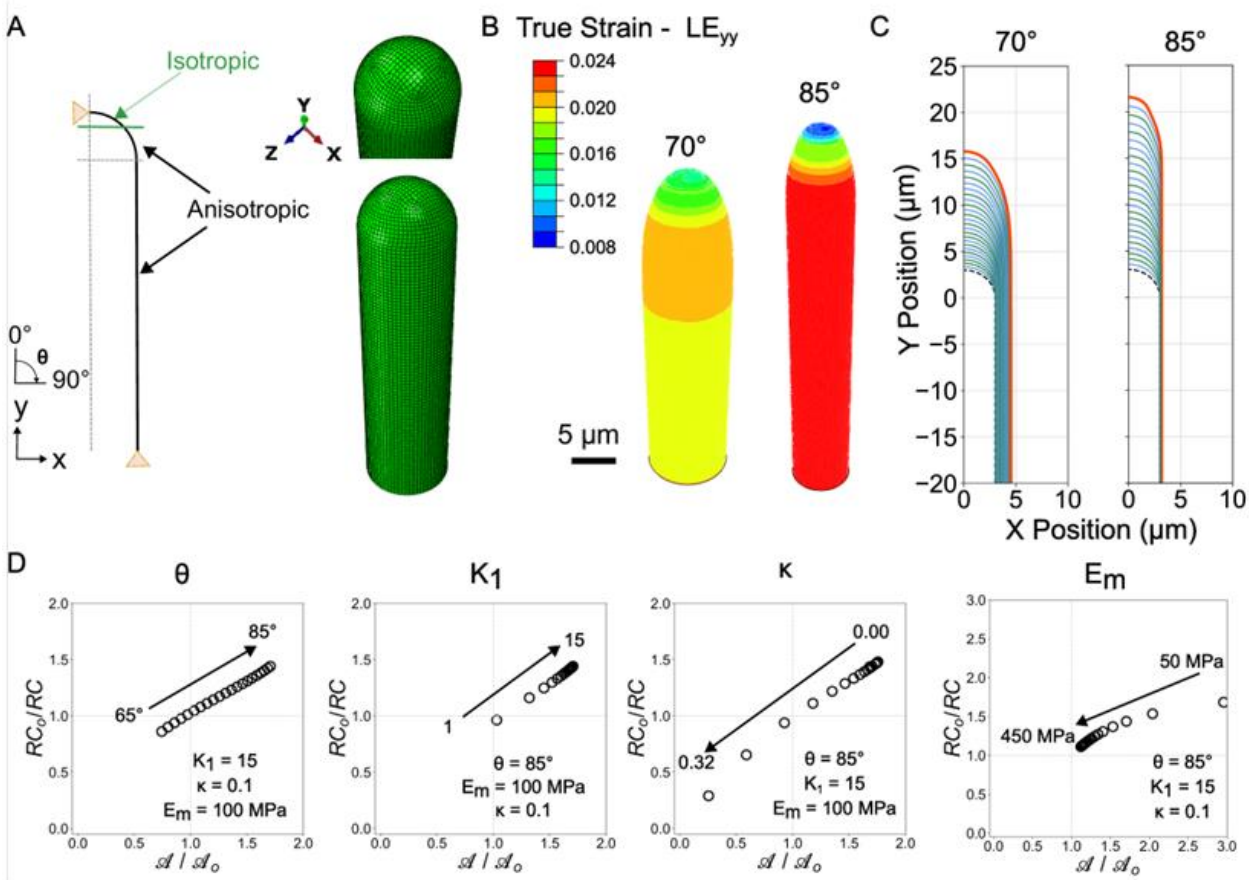

Figure 5: FE simulations with uniform material properties.
(A) Design of model geometry.
(B) Example true strain in axial direction on the 25th iteration of simulation with varied fiber angle. $K_1 = 15$, $\kappa = 0.1$, $E_m = 100$ MPa.
(C) Shape of fibers for 25 iterations with varied fiber angle. Black dashed line indicates initial shape. Orange line indicates final shape. Alternating blue and green lines indicate progressive iterations. $K_1 = 15$, $\kappa = 0.1$, $E_m = 100$ MPa.
(D) Normalized aspect ratio and inverse normalized radius of curvature for fibers with varied parameters. Open black circle indicates value after 25 iterations. Note the altered scale for E_m.

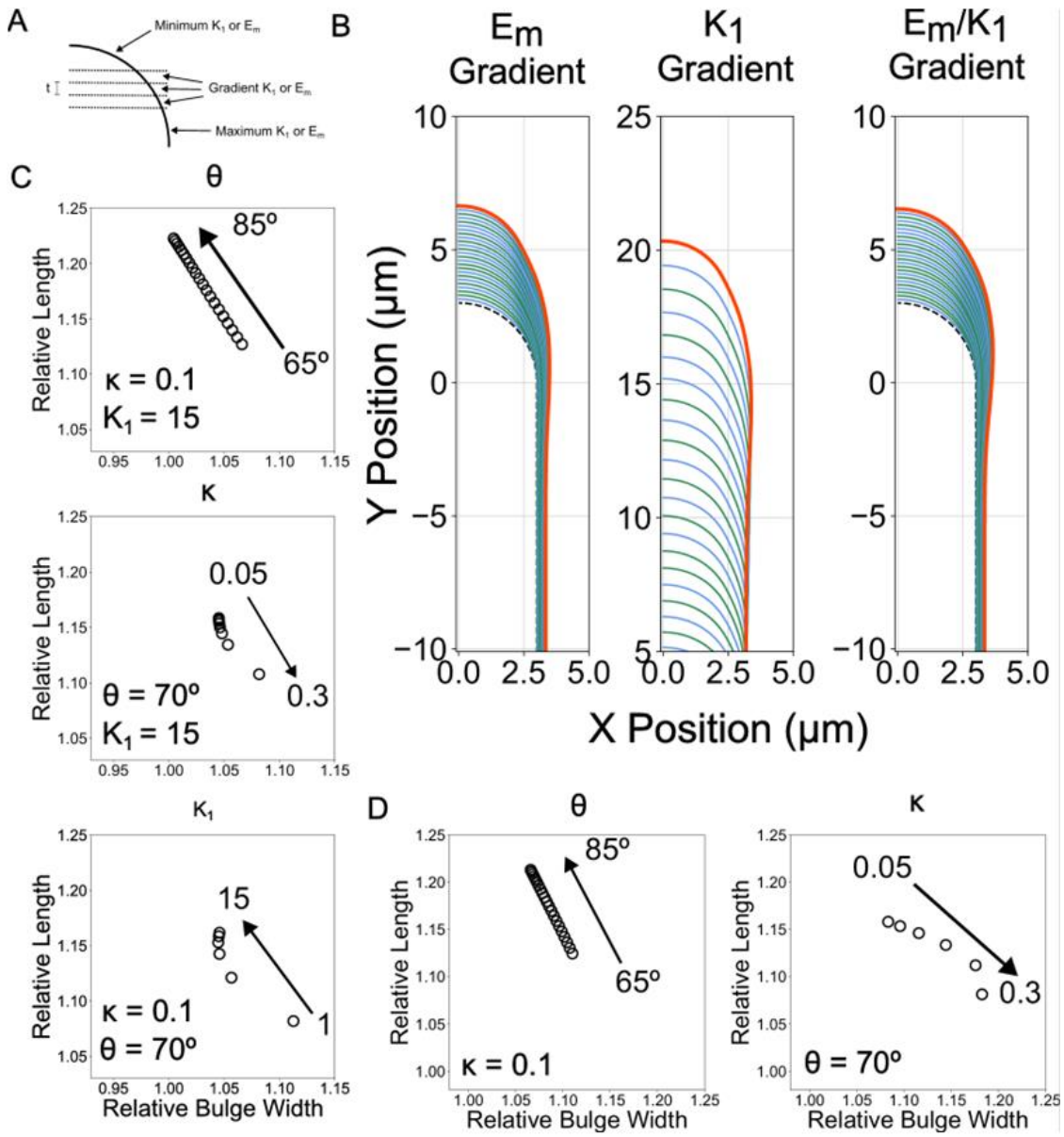

Figure 6: FE simulations with gradient material properties.
(A) Gradient design.
(B) Shape of fibers for 25 iterations with varied gradient type.
(C) Relative bulge width (X_{max} / X(y = -20)) and relative length (L_f / L_o) for fibers with varied parameters and E_m gradient. Open black circle indicates value after 25 iterations.
(D) Relative bulge width (X_{max} / X(y = -20)) and relative length (L_f / L_o) for fibers with varied parameters and E_m/K_1 gradient. Open black circle indicates value after 25 iterations

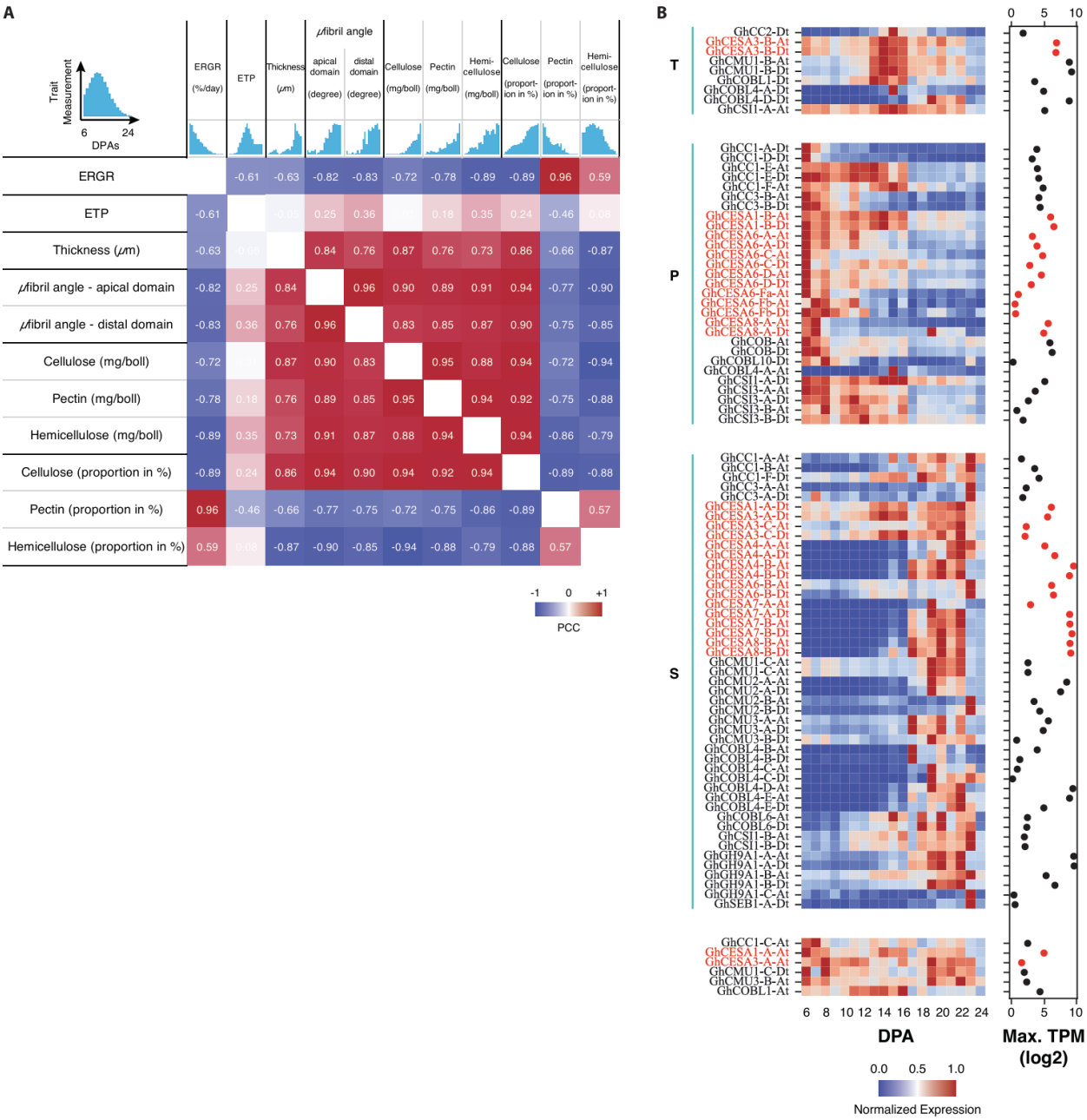

Figure 7: Integrated analysis of fiber phenotypes and candidate *G.h.* genes involved in cellulose synthesis.

(A) PCC analysis of fiber phenotypes.

(B) Expression variability of a cellulose synthesis gene expression module. Heat map of the expression levels of the fiber-expressed CESAs (highlighted red) and genes known to be involved in cellulose synthesis. Expression level was normalized from 0 to 1 for each gene and organized based on the timing of expression transitions and whether expression was trending down (P), transiently up (T), or trending up (S). P, contains many genes involved in primary cell wall synthesis, T, a transient state that marks a transition to SCW synthesis, S, SCW synthesis. To the right the maximum expression level for the gene across the entire developmental time course is shown, with red dots corresponding to CESA orthologs.

SUPPLEMENTAL FIGURE LEGENDS

Supplemental Figure 1. Polysaccharide content of cotton fiber cell walls during development (6 - 25 DPA). Cell wall was extracted from fibers and fractionated into pectin, hemicellulose and cellulose polysaccharides, dried, and weighed. The content of polysaccharides is presented as an absolute content (mg) per boll and also as proportion (%) in relation to other polysaccharides per boll in the graphs.
(A) Absolute cellulose content per boll from 6 to 25 DPA.
(B) Proportion of cellulose content per boll from 6 to 25 DPA.
(C) Absolute pectin content per boll from 6 to 25 DPA.
(D) Proportion of pectin content per boll from 6 to 25 DPA.
(E) Absolute hemicellulose content per boll from 6 to 25 DPA.
(F) Proportion of hemicellulose content per boll from 6 to 25 DPA. All the above data were mean ± SD of three biological replication bolls. Letters (a to i) indicate the significant differences among different DPA bolls (Fisher's LSD test, $p < 0.05$).

Supplemental Figure 2: All images collected and used for the analyses described in figures 1 & 2.
(A) Images at random locations along the length of the fibers.
(B) Images collected at the fiber tips.
Supplemental Figure 3. Ratio of tip diameter to minimum diameter from 6 to 24 DPA. Ratios between about 0.75 and 1.25 showed the expected, slightly tapered fiber phenotype. Fibers with a ratio around 0.5 generally had a constricted tip region with a swollen section just behind the tip. A ratio greater than 1.5 was indicative of a sock-shaped phenotype whereby the tip was swollen when compared to the more proximal regions of the fiber tip.

Supplemental Figure 3: Ratio of tip diameter to minimum diameter as a function of development. Select images are shown to depict different tip diameters.

Supplemental Figure 4: Local relationships between bundle spacing and cell shape.
(A-D) Region for comparison of bundle spacing within bulged (orange) or normal (blue) regions of fiber in random locations.
(E) Bundle spacing for parts A-D.
(F) Bundle density measured from 6 to 24 DPA.

REFERENCES

Applequist, W.L., Cronn, R. and Wendel, J.F. (2001). Comparative development of fiber in wild and cultivated cotton. Evol Dev. **3**, 3-17.
Avci, U., Pattathil, S., Singh, B., Brown, V.L., Hahn, M.G. and Haigler, C.H. (2013). Cotton fiber cell walls of Gossypium hirsutum and Gossypium barbadense have differences related to loosely-bound xyloglucan. PLoS One. **8**, e56315.

Baskin, T.I. (2005). Anisotropic expansion of the plant cell wall. Annu. Rev. Cell Dev. Biol. **21**, 203-222.
Basu, D., Le, J., El-Assal, S.E., Huang, S., Zhang, C., Mallery, E.L., Koliantz, G., Staiger, C.J. and Szymanski, D.B. (2005). DISTORTED3/SCAR2 is a putative Arabidopsis WAVE complex subunit that activates the Arp2/3 complex and is required for epidermal morphogenesis. Plant Cell. **17**, 502-524.
Beasley, C. and Ting, I. (1974). Effects of plant growth substances on in vitro fiber development from unfertilized cotton ovules. Am. J. Bot. **61**, 188-194.
Belteton, S., Li, W., Hatam, F.A., Quinn, M.I., Szymanski, M.R., Marley, M., Turner, J.A. and Szymanski, D.B. (2021). Real-time conversion of tissue-scale mechanical forces into an interdigitated growth pattern. Nature Plants. **7**, 826-841.
Benfey, P.N., Linstead, P.J., Roberts, K., Schiefelbein, J.W., Hauser, M.T. and Aeschbacher, R.A. (1993). Root development in Arabidopsis: four mutants with dramatically altered root morphogenesis. Development. **119**, 57-70.
Betancur, L., Singh, B., Rapp, R.A., Wendel, J.F., Marks, M.D., Roberts, A.W. and Haigler, C.H. (2010). Phylogenetically distinct cellulose synthase genes support secondary wall thickening in arabidopsis shoot trichomes and cotton fiber. Journal of integrative plant biology. **52**, 205-220.
Bidhendi, A.J. and Geitmann, A. (2018). Finite Element Modeling of Shape Changes in Plant Cells. Plant physiology. **176**, 41-56.
Buschmann, H. and Lloyd, C.W. (2008). *Arabidopsis* mutants and the network of microtubule-associated functions. Mol. Plant. **1**, 888-898.
Chan, J. and Coen, E. (2020). Interaction between Autonomous and Microtubule Guidance Systems Controls Cellulose Synthase Trajectories. Curr Biol. **30**, 941-947 e942.
Cosgrove, D.J. (2000). Expansive growth of plant cell walls. Plant Physiology and Biochemistry. **38**, 1-16.
Cosgrove, D.J. (2024). Plant Cell Wall Loosening by Expansins. Annual Review of Cell and Developmental Biology. **40**,
Crowell, E.F., Timpano, H., Desprez, T., Franssen-Verheijen, T., Emons, A.M., Hofte, H. and Vernhettes, S. (2011). Differential regulation of cellulose orientation at the inner and outer face of epidermal cells in the Arabidopsis hypocotyl. Plant Cell. **23**, 2592-2605.
Elliott, A. and Shaw, S.L. (2018). Microtubule Array Patterns Have a Common Underlying Architecture in Hypocotyl Cells. Plant Physiol. **176**, 307-325.
Fang, D.D., Naoumkina, M. and Kim, H.J. (2018). Unraveling cotton fiber development using fiber mutants in the post-genomic era. Crop Science. **58**, 2214-2228.
Fayant, P., Girlanda, O., Chebli, Y., Aubin, C.E., Villemure, I. and Geitmann, A. (2010). Finite element model of polar growth in pollen tubes. Plant Cell. **22**, 2579-2593.
Gasser, T.C., Ogden, R.W. and Holzapfel, G.A. (2006). Hyperelastic modelling of arterial layers with distributed collagen fibre orientations. J R Soc Interface. **3**, 15-35.
Gilbert, M.K., Kim, H.J., Tang, Y., Naoumkina, M. and Fang, D.D. (2014). Comparative transcriptome analysis of short fiber mutants Ligon-lintless 1 and 2 reveals common mechanisms pertinent to fiber elongation in cotton (Gossypium hirsutum L.). PLoS One. **9**, e95554.
Graham, B.P. and Haigler, C.H. (2021). Microtubules exert early, partial, and variable control of cotton fiber diameter. Planta. **253**, 47.

Green, P.B. and King, A. (1966). A Mechanism for Origin of Specifically Oriented Textures in Development with Special Reference to Nitella Wall Texture. Australian Journal of Biological Sciences. **19**, 421-&.
Grover, C.E., Jareczek, J.J., Swaminathan, S., Lee, Y., Howell, A.H., Rani, H., Arick, M.A., Leach, A.G., Miller, E.R., Yang, P., Hu, G., Xiong, X., Mallery, E.L., Peterson, D.G., Xie, J., Haigler, C.H., Zabotina, O.A., Szymanski, D.B. and Wendel, J.F. (2024). A high-resolution model of gene expression during Gossypium hirsutum (cotton) fiber development. bioRxiv. 2024.2007.2020.604417.
Gu, Y., Kaplinsky, N., Bringmann, M., Cobb, A., Carroll, A., Sampathkumar, A., Baskin, T.I., Persson, S. and Somerville, C.R. (2010). Identification of a cellulose synthase-associated protein required for cellulose biosynthesis. Proc. Natl. Acad. Sci. U.S.A. **107**, 12866-12871.
Gu, Y. and Rasmussen, C.G. (2022). Cell biology of primary cell wall synthesis in plants. Plant Cell. **34**, 103-128.
Haigler, C.H., Singh, B., Wang, G. and Zhang, D. (2009). Genomics of cotton fiber secondary wall deposition and cellulose biogenesis. Genetics and genomics of cotton. 385-417.
Hamant, O., Heisler, M.G., Jonsson, H., Krupinski, P., Uyttewaal, M., Bokov, P., Corson, F., Sahlin, P., Boudaoud, A., Meyerowitz, E.M. and Traas, J. (2008). Developmental patterning by mechanical signals in *Arabidopsis*. Science. **322**, 1650-1655.
Hejnowicz, Z., Rusin, A. and Rusin, T. (2000). Tensile Tissue Stress Affects the Orientation of Cortical Microtubules in the Epidermis of Sunflower Hypocotyl. J Plant Growth Regul. **19**, 31-44.
Himmelspach, R., Williamson, R.E. and Wasteneys, G.O. (2003). Cellulose microfibril alignment recovers from DCB-induced disruption despite microtubule disorganization. Plant Journal. **36**, 565-575.
Holzapfel, G.A., Gasser, T.C. and Ogden, R.W. (2000). A new constitutive framework for arterial wall mechanics and a comparative study of material models. Journal of elasticity and the physical science of solids. **61**, 1-48.
Hsieh, Y.-L. (2007). Chemical structure and properties of cotton. Cotton: Science and technology. 3-34.
Jiang, J., Shi, Z., Ma, F. and Liu, K. (2022). Identification of key proteins related to high-quality fiber in Upland cotton via proteomics analysis. Plant Cell Rep. **41**, 893-904.
Kesten, C., Wallmann, A., Schneider, R., McFarlane, H.E., Diehl, A., Khan, G.A., van Rossum, B.J., Lampugnani, E.R., Szymanski, W.G., Cremer, N., Schmieder, P., Ford, K.L., Seiter, F., Heazlewood, J.L., Sanchez-Rodriguez, C., Oschkinat, H. and Persson, S. (2019). The companion of cellulose synthase 1 confers salt tolerance through a Tau-like mechanism in plants. Nature Communications. **10**,
Keynia, S., Davis, T.C., Szymanski, D.B. and Turner, J.A. (2022). Cell twisting during desiccation reveals axial asymmetry in wall organization. Biophysical Journal. **121**, 932-942.
Kierzkowski, D. and Routier-Kierzkowska, A.-L. (2019). Cellular basis of growth in plants: geometry matters. Current Opinion in Plant Biology. **47**, 56-63.
Kim, H.J., Murai, N., Fang, D.D. and Triplett, B.A. (2011). Functional analysis of Gossypium hirsutum cellulose synthase catalytic subunit 4 promoter in transgenic Arabidopsis and cotton tissues. Plant Sci. **180**, 323-332.
Kumar, M., Campbell, L. and Turner, S. (2016). Secondary cell walls: biosynthesis and manipulation. Journal of Experimental Botany. **67**, 515-531.

Lee, Y. (unpublished). Proteomics analysis for understanding primary controls of cotton fiber development.
Li, X.B., Fan, X.P., Wang, X.L., Cai, L. and Yang, W.C. (2005). The cotton ACTIN1 gene is functionally expressed in fibers and participates in fiber elongation. Plant Cell. **17**, 859-875.
Liu, Z., Schneider, R., Kesten, C., Zhang, Y., Somssich, M., Zhang, Y., Fernie, A.R. and Persson, S. (2016). Cellulose-Microtubule Uncoupling Proteins Prevent Lateral Displacement of Microtubules during Cellulose Synthesis in Arabidopsis. Dev Cell. **38**, 305-315.
Lockhart, J.A. (1965). An analysis of irreversible plant cell elongation. Journal of Theoretical Biology. **8**, 264-275.
Lyczakowski, J.J., Bourdon, M., Terrett, O.M., Helariutta, Y., Wightman, R. and Dupree, P. (2019). Structural Imaging of Native Cryo-Preserved Secondary Cell Walls Reveals the Presence of Macrofibrils and Their Formation Requires Normal Cellulose, Lignin and Xylan Biosynthesis. Frontiers in plant science. **10**,
MacMillan, C.P., Birke, H., Chuah, A., Brill, E., Tsuji, Y., Ralph, J., Dennis, E.S., Llewellyn, D. and Pettolino, F.A. (2017). Tissue and cell-specific transcriptomes in cotton reveal the subtleties of gene regulation underlying the diversity of plant secondary cell walls. BMC Genomics. **18**, 539.
Martinez-Sanz, M., Pettolino, F., Flanagan, B., Gidley, M.J. and Gilbert, E.P. (2017). Structure of cellulose microfibrils in mature cotton fibres. Carbohydr Polym. **175**, 450-463.
Meinert, M.C. and Delmer, D.P. (1977). Changes in biochemical composition of the cell wall of the cotton fiber during development. Plant Physiol. **59**, 1088-1097.
Nicol, F., His, I., Jauneau, A., Vernhettes, S., Canut, H. and Hofte, H. (1998). A plasma membrane-bound putative endo-1,4-beta-D-glucanase is required for normal wall assembly and cell elongation in Arabidopsis. EMBO Journal. **17**, 5563-5576.
Nixon, B.T., Mansouri, K., Singh, A., Du, J., Davis, J.K., Lee, J.G., Slabaugh, E., Vandavasi, V.G., O'Neill, H., Roberts, E.M., Roberts, A.W., Yingling, Y.G. and Haigler, C.H. (2016). Comparative Structural and Computational Analysis Supports Eighteen Cellulose Synthases in the Plant Cellulose Synthesis Complex. Sci Rep. **6**, 28696.
Oda, Y. (2015). Cortical microtubule rearrangements and cell wall patterning. Frontiers in plant science. **6**, 236.
Paredez, A.R., Somerville, C.R. and Ehrhardt, D.W. (2006). Visualization of cellulose synthase demonstrates functional association with microtubules. Science. **312**, 1491-1495.
Pear, J.R., Kawagoe, Y., Schreckengost, W.E., Delmer, D.P. and Stalker, D.M. (1996). Higher plants contain homologs of the bacterial celA genes encoding the catalytic subunit of cellulose synthase. Proc. Natl. Acad. Sci. U.S.A. **93**, 12637-12642.
Pettolino, F.A., Yulia, D., Bacic, A. and Llewellyn, D.J. (2022). Polysaccharide composition during cotton seed fibre development: temporal differences between species and in different seasons. Journal of Cotton Research. **5**,
Polko, J.K. and Kieber, J.J. (2019). The Regulation of Cellulose Biosynthesis in Plants. Plant Cell. **31**, 282-296.
Proseus, T.E., Zhu, G.L. and Boyer, J.S. (2000). Turgor, temperature and the growth of plant cells: using Chara corallina as a model system. J Exp Bot. **51**, 1481-1494.
Purushotham, P., Ho, R. and Zimmer, J. (2020). Architecture of a catalytically active homotrimeric plant cellulose synthase complex. Science. **369**, 1089-1094.

Qin, Y.M. and Zhu, Y.X. (2011). How cotton fibers elongate: a tale of linear cell-growth mode. Curr Opin Plant Biol. **14**, 106-111.
Qu, J., Ye, J., Geng, Y.F., Sun, Y.W., Gao, S.Q., Zhang, B.P., Chen, W. and Chua, N.H. (2012). Dissecting functions of KATANIN and WRINKLED1 in cotton fiber development by virus-induced gene silencing. Plant Physiol. **160**, 738-748.
Roudier, F., Fernandez, A.G., Fujita, M., Himmelspach, R., Borner, G.H., Schindelman, G., Song, S., Baskin, T.I., Dupree, P., Wasteneys, G.O. and Benfey, P.N. (2005). COBRA, an Arabidopsis Extracellular Glycosyl-Phosphatidyl Inositol-Anchored Protein, Specifically Controls Highly Anisotropic Expansion through Its Involvement in Cellulose Microfibril Orientation. Plant Cell. **17**, 1749-1763.
Ruan, Y.-L., Xu, S.-M., White, R. and Furbank, R.T. (2004). Genotypic and developmental evidence for the role of plasmodesmatal regulation in cotton fiber elongation mediated by callose turnover. Plant physiology. **136**, 4104-4113.
Ruan, Y., Llewellyn, D. and Furbank, R. (2001). The control of single-celled cotton fiber elongation by developmentally reversible gating of plasmodesmata and coordinated expression of sucrose and k(+) transporters and expansin. Plant Cell. **13**, 47-60.
Ryser, U. (1977). Cell-Wall Growth in Elongating Cotton Fibers - Autoradiographic Study. Cytobiologie. **15**, 78-84.
Sambade, A., Findlay, K., Schaffner, A.R., Lloyd, C.W. and Buschmann, H. (2014). Actin-dependent and -independent functions of cortical microtubules in the differentiation of Arabidopsis leaf trichomes. Plant Cell. **26**, 1629-1644.
Schindelin, J., Arganda-Carreras, I., Frise, E., Kaynig, V., Longair, M., Pietzsch, T., Preibisch, S., Rueden, C., Saalfeld, S. and Schmid, B. (2012). Fiji: an open-source platform for biological-image analysis. Nature methods. **9**, 676-682.
Schindelman, G., Morikami, A., Jung, J., Baskin, T.I., Carpita, N.C., Derbyshire, P., McCann, M.C. and Benfey, P.N. (2001). COBRA encodes a putative GPI-anchored protein, which is polarly localized and necessary for oriented cell expansion in Arabidopsis. Genes & Development. **15**, 1115-1127.
Schubert, A.M., Benedict, C.R., Berlin, J.D. and Kohel, R.J. (1973). Cotton Fiber Development - Kinetics of Cell Elongation and Secondary Wall Thickening. Crop Science. **13**, 704-709.
Schubert, A.M., Benedict, C.R., Gates, C.E. and Kohel, R.J. (1976). Growth and Development of Lint Fibers of Pima S-4 Cotton. Crop Science. **16**, 539-543.
Seagull, R.W. (1986). Changes in microtubule organization an wall microfibril orientation during *in vitro* cotton fiber development: an immunofluorescent study. Can. J. Bot. **64**, 1373-1381.
Seagull, R.W. (1986). Changes in microtubule organization and wall microfibril orientation during in vitro cotton fiber development: an immunofluroescent study. Can J Bot. **64**, 1373-1381.
Seagull, R.W. (1993). Cytoskeletal Involvement in Cotton Fiber Growth and Development. Micron. **24**, 643-660.
Seagull, R.W. (1990). The effects of microtubule and microfilament disrupting agents on cytoskeletal arrays and wall deposition in developing cotton fibers. Protoplasma. **159**, 44-59.
Seagull, R.W. (1992). A Quantitative Electron-Microscopic Study of Changes in Microtubule Arrays and Wall Microfibril Orientation during Invitro Cotton Fiber Development. Journal of Cell Science. **101**, 561-577.

Sonnhammer, E.L. and Ostlund, G. (2015). InParanoid 8: orthology analysis between 273 proteomes, mostly eukaryotic. Nucleic Acids Res. **43**, D234-239.
Stiff, M.R. and Haigler, C.H. (2016). Cotton fiber tips have diverse morphologies and show evidence of apical cell wall synthesis. Sci Rep. **6**, 27883.
Swaminathan, S., Grover, C.E., Mugisha, A.S., Sichterman, L.E., Lee, Y., Yang, P., Mallery, E.L., Jareczek, J.J., Leach, A.G., Xie, J., Wendel, J.F., Szymanski, D.B. and Zabotina, O.A. (2024). Daily glycome and transcriptome profiling reveals polysaccharide structures and glycosyltransferases critical for cotton fiber growth. bioRxiv. 2024.2004.2023.589927.
Szymanski, D.B. and Cosgrove, D.J. (2009). Dynamic coordination of cytoskeletal and cell wall systems during plant cell morphogenesis. Curr. Biol. **19**, R800-R811.
Szymanski, D.B. and Staiger, C.J. (2018). The actin cytoskeleton: functional arrays for cytoplasmic organization and cell shape control. Plant Physiol. **176**, 106-118.
Thyssen, G.N., Fang, D.D., Turley, R.B., Florane, C.B., Li, P., Mattison, C.P. and Naoumkina, M. (2017). A Gly65Val substitution in an actin, GhACT_LI1, disrupts cell polarity and F-actin organization resulting in dwarf, lintless cotton plants. Plant J. **90**, 111-121.
Tiwari, S.C. and Wilkins, T.A. (1995). Cotton (*Gossypium hirsutum*) seed trichomes expand via diffuse growing mechanism. Can. J. Bot. **73**, 746-757.
Tuttle, J.R., Nah, G., Duke, M.V., Alexander, D.C., Guan, X.Y., Song, Q.X., Chen, Z.J., Scheffler, B.E. and Haigler, C.H. (2015). Metabolomic and transcriptomic insights into how cotton fiber transitions to secondary wall synthesis, represses lignification, and prolongs elongation. Bmc Genomics. **16**,
Urbanowicz, B.R., Bennett, A.B., Del Campillo, E., Catala, C., Hayashi, T., Henrissat, B., Hofte, H., McQueen-Mason, S.J., Patterson, S.E., Shoseyov, O., Teeri, T.T. and Rose, J.K. (2007). Structural organization and a standardized nomenclature for plant endo-1,4-beta-glucanases (cellulases) of glycosyl hydrolase family 9. Plant Physiol. **144**, 1693-1696.
Uyttewaal, M., Burian, A., Alim, K., Landrein, B., Borowska-Wykret, D., Dedieu, A., Peaucelle, A., Ludynia, M., Traas, J., Boudaoud, A., Kwiatkowska, D. and Hamant, O. (2012). Mechanical stress acts via katanin to amplify differences in growth rate between adjacent cells in Arabidopsis. Cell. **149**, 439-451.
Williamson, R.E. (1990). Alignment of Cortical Microtubules by Anisotropic Wall Stresses. Australian Journal of Plant Physiology. **17**, 601-613.
Yanagisawa, M., Desyatova, A.S., Belteton, S., Mallery, E.M., Turner, J.A. and Szymanski, D.B. (2015). Patterning mechanisms of cytoskeletal and cell wall systems during leaf trichome morphogenesis. Nature Plant. **1**, 15014.
Yanagisawa, M., Keynia, S., Belteton, S., Turner, J.A. and Szymanski, D.B. (2022). A conserved cellular mechanism for cotton fibre diameter and length control. . *in silico* Plants. **4**,
Yu, Y., Wu, S., Nowak, J., Wang, G., Han, L., Feng, Z., Mendrinna, A., Ma, Y., Wang, H., Zhang, X., Tian, J., Dong, L., Nikoloski, Z., Persson, S. and Kong, Z. (2019). Live-cell imaging of the cytoskeleton in elongating cotton fibres. Nat Plants. **5**, 498-504.
Zang, Y., Hu, Y., Xu, C., Wu, S., Wang, Y., Ning, Z., Han, Z., Si, Z., Shen, W., Zhang, Y., Fang, L. and Zhang, T. (2021). GhUBX controlling helical growth results in production of stronger cotton fiber. iScience. **24**, 102930.
Zhang, X., Dyachok, J., Krishnakumar, S., Smith, L.G. and Oppenheimer, D.G. (2005). IRREGULAR TRICHOME BRANCH1 in Arabidopsis encodes a plant homolog of the actin-related

protein2/3 complex activator Scar/WAVE that regulates actin and microtubule organization. Plant Cell. **17**, 2314-2326.
Zhang, Y., Yu, J., Wang, X., Durachko, D.M., Zhang, S. and Cosgrove, D.J. (2021). Molecular insights into the complex mechanics of plant epidermal cell walls. Science. **372**, 706-711.
Zhong, R., Cui, D. and Ye, Z.H. (2019). Secondary cell wall biosynthesis. New Phytol. **221**, 1703-1723.